The Extraordinary March 2022 East Antarctica “Heat” Wave. Part II: Impacts on the Antarctic Ice Sheet

JONATHAN D. WILLE,[a,b] SIMON P. ALEXANDER,[c,d] CHARLES AMORY,[a] REBECCA BAIMAN,[e] LÉONARD BARTHÉLEMY,[f]
DANA M. BERGSTROM,[c,g,h] ALEXIS BERNE,[i] HANIN BINDER,[b] JULIETTE BLANCHET,[a] DENIZ BOZKURT,[j,k]
THOMAS J. BRACEGIRDLE,[l] MATHIEU CASADO,[m] TAEJIN CHOI,[n] KYLE R. CLEM,[o] FRANCIS CODRON,[f]
RAJASHREE DATTA,[c] STEFANO DI BATTISTA,[p] VINCENT FAVIER,[a] DIANA FRANCIS,[q] ALEXANDER D. FRASER,[d]
ELISE FOURRÉ,[m] RENÉ D. GARREAUD,[k,r] CHRISTOPHE GENTHON,[s] IRINA V. GORODETSKAYA,[t]
SERGI GONZÁLEZ-HERRERO,[u,v] VICTORIA J. HEINRICH,[w] GUILLAUME HUBERT,[x] HANNA JOOS,[b]
SEONG-JOONG KIM,[n] JOHN C. KING,[l] CHRISTOPH KITTEL,[a] AMAELLE LANDAIS,[m] MATTHEW LAZZARA,[y,z]
GREGORY H. LEONARD,[aa] JAN L. LIESER,[bb] MICHELLE MACLENNAN,[e] DAVID MIKOLAJCZYK,[y] PETER NEFF,[cc]
INÈS OLLIVIER,[dd,m] GHISLAIN PICARD,[a] BENJAMIN POHL,[ee] F. MARTIN RALPH,[ff] PENNY ROWE,[gg]
ELISABETH SCHLOSSER,[hh] CHRISTINE A. SHIELDS,[ii] INGA J. SMITH,[jj] MICHAEL SPRENGER,[b] LUKE TRUSEL,[kk]
DANIELLE UDY,[d,bb,ll] TESSA VANCE,[d] ÉTIENNE VIGNON,[s] CATHERINE WALKER,[mm] NANDER WEVER,[e,u] AND XUN ZOU[ff]

[a] *Institut des Géosciences de l’Environnement, CNRS/UGA, Saint Martin d’Hères, France*
[b] *Institute for Atmospheric and Climate Science, ETH Zurich, Zurich, Switzerland*
[c] *Australian Antarctic Division, Kingston, Tasmania, Australia*
[d] *Australian Antarctic Program Partnership, Institute for Marine and Antarctic Studies, University of Tasmania, Hobart, Tasmania, Australia*
[e] *Department of Atmospheric and Oceanic Sciences, University of Colorado Boulder, Boulder, Colorado*
[f] *Laboratoire d’Océanographie et du Climat, LOCEAN-IPSL, Sorbonne Université, CNRS, IRD, MNHN, Paris, France*
[g] *Global Challenges Program, University of Wollongong, Wollongong, New South Wales, Australia*
[h] *Centre for Ecological Genomics and Wildlife Conservation, Department of Zoology, University of Johannesburg, Johannesburg, South Africa*
[i] *Environmental Remote Sensing Laboratory (LTE), École Polytechnique Fédérale de Lausanne, Lausanne, Switzerland*
[j] *Department of Meteorology, University of Valparaíso, Valparaíso, Chile*
[k] *Center for Climate and Resilience Research, Santiago, Chile*
[l] *British Antarctic Survey, Cambridge, United Kingdom*
[m] *Laboratoire des Sciences du Climat et de l’Environnement, CNRS-CEA-UVSQ-IPSL, Gif sur Yvette, France*
[n] *Korea Polar Research Institute, Incheon, South Korea*
[o] *School of Geography, Environment and Earth Sciences, Victoria University of Wellington, Wellington, New Zealand*
[p] *Meteogiornale, Milan, Italy*
[q] *Environmental and Geophysical Sciences (ENGEOS) Lab, Khalifa University, Abu Dhabi, United Arab Emirates*
[r] *Universidad de Chile, Santiago, Chile*
[s] *LMD/IPSL, Sorbonne Université, ENS, PSL Research University, École Polytechnique, Institut Polytechnique de Paris, CNRS, Paris, France*
[t] *CIIMAR–Interdisciplinary Centre of Marine and Environmental Research of the University of Porto, Porto, Portugal*
[u] *WSL Institute for Snow and Avalanche Research SLF, Davos, Switzerland*
[v] *Antarctic Group, Agencia Estatal de Meteorología (AEMET), Barcelona, Spain*
[w] *School of Psychological Sciences, University of Tasmania, Hobart, Tasmania, Australia*
[x] *The French Aerospace Lab, ONERA/DPHY, University of Toulouse, Toulouse, France*
[y] *Antarctic Meteorological Research and Data Center, Space Science and Engineering Center, University of Wisconsin–Madison, Madison, Wisconsin*
[z] *Department of Physical Sciences, School of Engineering, Science, and Mathematics, Madison Area Technical College, Madison, Wisconsin*
[aa] *National School of Surveying, University of Otago, Dunedin, New Zealand*
[bb] *Institute for Marine and Antarctic Studies, University of Tasmania, Hobart, Tasmania, Australia*
[cc] *University of Minnesota, Saint Paul, Minnesota*
[dd] *Bjerknes Centre for Climate Research, University of Bergen, Bergen, Norway*
[ee] *Biogéosciences, CNRS/Université de Bourgogne, Dijon, France*
[ff] *Center for Western Weather and Water Extremes, Scripps Institution of Oceanography, San Diego, California*
[gg] *NorthWest Research Associates, Seattle, Washington*
[hh] *Department of Atmospheric and Cryospheric Sciences, University of Innsbruck, Innsbruck, Austria*
[ii] *Climate and Global Dynamics Laboratory, National Center for Atmospheric Research, Boulder, Colorado*
[jj] *Department of Physics, University of Otago, Dunedin, New Zealand*
[kk] *Department of Geography, The Pennsylvania State University, University Park, Pennsylvania*
[ll] *ARC Centre of Excellence for Climate Extremes, University of Tasmania, Hobart, Tasmania, Australia*
[mm] *Department of Applied Ocean Physics and Engineering, Woods Hole Oceanographic Institution, Woods Hole, Massachusetts*

Supplemental information related to this paper is available at the Journals Online website: https://doi.org/10.1175/JCLI-D-23-0176.s1.

Corresponding author: Jonathan D. Wille, jonathan.wille@env.ethz.ch

DOI: 10.1175/JCLI-D-23-0176.1

(Manuscript received 27 March 2023, in final form 25 October 2023, accepted 30 October 2023)

ABSTRACT: Between 15 and 19 March 2022, East Antarctica experienced an exceptional heat wave with widespread 30°–40°C temperature anomalies across the ice sheet. In Part I, we assessed the meteorological drivers that generated an intense atmospheric river (AR) that caused these record-shattering temperature anomalies. Here, we continue our large collaborative study by analyzing the widespread and diverse impacts driven by the AR landfall. These impacts included widespread rain and surface melt that was recorded along coastal areas, but this was outweighed by widespread high snowfall accumulations resulting in a largely positive surface mass balance contribution to the East Antarctic region. An analysis of the surface energy budget indicated that widespread downward longwave radiation anomalies caused by large cloud-liquid water contents along with some scattered solar radiation produced intense surface warming. Isotope measurements of the moisture were highly elevated, likely imprinting a strong signal for past climate reconstructions. The AR event attenuated cosmic ray measurements at Concordia, something previously never observed. Last, an extratropical cyclone west of the AR landfall likely triggered the final collapse of the critically unstable Conger Ice Shelf while further reducing an already record low sea ice extent.

SIGNIFICANCE STATEMENT: Using our diverse collective expertise, we explored the impacts from the March 2022 heat wave and atmospheric river across East Antarctica. One key takeaway is that the Antarctic cryosphere is highly sensitive to meteorological extremes originating from the midlatitudes and subtropics. Despite the large positive temperature anomalies driven from strong downward longwave radiation, this event led to huge amounts of snowfall across the Antarctic interior desert. The isotopes in this snow of warm airmass origin will likely be detectable in future ice cores and potentially distort past climate reconstructions. Even measurements of space activity were affected. Also, the swells generated from this storm helped to trigger the final collapse of an already critically unstable Conger Ice Shelf while further degrading sea ice coverage.

KEYWORDS: Antarctica; Ice shelves; Snow; Energy budget/balance; Paleoclimate

1. Introduction

Between 15 and 19 March 2022, East Antarctica experienced an unprecedented heat wave with widespread 30°–40°C temperature anomalies peaking on 18 March where record-high maximum temperatures were observed from coastal regions like Dumont d'Urville to the high Antarctic Plateau like Dome C and Vostok. In the first part of this study (Wille et al. 2024, hereinafter Part I), we analyzed the large-scale drivers of that event, as well as its temperature response over the East Antarctic Ice Sheet. These austral autumnal March temperature extremes rivaled record-high maximum temperatures observed during peak summer, which is very unusual because the Antarctic climate is usually quickly transitioning to winter conditions in March. In Part I, we established that this event was caused by a very intense and persistent atmospheric river (AR; Ralph et al. 2020) accompanied by a very strong atmospheric ridge throughout the depth of the troposphere (Part I). The high pressure system was enhanced by and contributed in return to channel subtropical/midlatitude heat and moisture deep into the plateau of East Antarctica. As the heat-wave event unfolded, relatively heavy snowfalls were observed on the plateau, rain and modest surface melting were observed along some coastal regions, and the small Conger Ice Shelf collapsed. In this second part of our study, we propose to analyze the impacts of this major event on the environment of East Antarctica.

ARs have been shown to cause strong positive anomalies of temperature and humidity across Antarctica (Gorodetskaya et al. 2020; Turner et al. 2022b) and significant mass balance impacts over the Antarctic ice sheet (Wille et al. 2019, 2022, 2021; Adusumilli et al. 2021; Bozkurt et al. 2018; Gehring et al. 2022; Gorodetskaya et al. 2014; Maclennan et al. 2022b,a). Their impacts on surface mass balance range from surface melt induced by enhanced cloud liquid water content and radiative forcing (e.g., in West Antarctica; Wille et al. 2019; Adusumilli et al. 2021; Djoumna and Holland 2021) to ice-shelf instability from surface melt, ocean swell processes, and storm surge (Wille et al. 2022; Francis et al. 2021), and intense snowfall events in East Antarctica that control interannual precipitation variability (Wille et al. 2021; Gorodetskaya et al. 2014). All of the previously documented AR impacts were observed during this heat-wave event, but its duration and its intensity as defined by integrated vapor transport (IVT), unprecedented since the beginning of the satellite era, contributed to make it a record-breaking event in multiple areas.

Globally in this study (Part I and this paper), we present a detailed analysis of the heat wave's origins and review the multitude of impacts across East Antarctica in order to encapsulate the event's historical nature. We unravel the various atmospheric processes and impacts interacting with one another during this compound event. This is done by combining numerous different datasets and expertise to provide a comprehensive analysis/overview of the March 2022 East Antarctic heat wave and place this event in context with other extreme Antarctic climate events observed. In this paper, we describe the various impacts on the ice sheet; the overall impacts on the surface mass balance and near surface firn (section 3); the causality between the AR/heat wave and the collapse of the Conger Ice Shelf along with other sea ice impacts (section 4); and the mass balance and paleoclimate dating-relevant signatures on the East Antarctic ice sheet (section 5). We discuss the event's influences on cosmic ray and paleoclimate measurements (section 6a), concluding with a discussion on the implications of this heat wave for the future Antarctic climate system and the risks of such an event happening more frequently in a warming climate (section 6b).

2. Data and methods

a. Precipitation, melt, and moisture products

To quantify the precipitation associated with the event, we first used MERRA-2 and ERA5 atmospheric reanalysis data. To determine the total amount of precipitation associated with the AR/heat-wave event, we integrate precipitation over the Antarctic Ice Sheet (grounded ice and ice shelves) from 14 to 18 March, and for the whole month of March 2022. We compare this event-attributed precipitation with the mean total precipitation in March from 1980 to 2021. To improve our estimates, we also used melt and precipitation (rainfall and snowfall) during the event from the high-resolution (35-km horizontal gridding) regional climate model Modèle Atmosphérique Régional (MAR), version 3.11 (referred to simply as MAR hereinafter), in its Antarctic setup (Agosta et al. 2019) with the updates described in Kittel et al. (2021). MAR is driven at its lateral boundaries (pressure, wind speed, temperature, specific humidity), at the top of the troposphere (temperature, wind speed) and at the ocean surface (sea ice concentration, sea surface temperature) by 6-hourly ERA5 reanalysis, and evolves freely in its inner spatial domain, including the snowpack and firn layer. The polar-oriented model physics allows a detailed representation of the interactions between the Antarctic boundary layer, snowfall, and the firn layer, yielding similar snow accumulation rates at the surface irrespective of the driving reanalysis (Agosta et al. 2019). We use MAR rather than reanalysis data because the model has been more extensively evaluated over the continent and shown to be able to reproduce the observed variability in near-surface climate and surface mass balance at the employed resolution (Mottram et al. 2021).

b. Vertical profile measurements from Dumont d'Urville

At Dumont d'Urville (DDU) station, the evolution of the AR and of the associated landfall was analyzed using radiosonde data following the processing methodology of Vignon et al. (2019). To characterize the vertical structure of the precipitation during the AR, we used data collected by a Micro Rain Radar (MRR) deployed under a radome at the station in 2015. The MRR provides vertical profiles of K-band (24 GHz) reflectivity and Doppler velocity over the first 3000 m above ground level (AGL) with a resolution of 100 m. Data were processed following the processing chain for snow hydrometeors developed by Maahn and Kollias (2012) and the attenuation due to the radome was estimated and corrected following Grazioli et al. (2017). Further details on the instrument deployment and data processing are provided in Grazioli et al. (2017) and Durán-Alarcón et al. (2019). In addition, we characterized the evolution of the cloud base altitude during the AR using data from a Vaisala, Inc., CL-31 ceilometer deployed in 2020.

c. Surface snow modeling

To analyze the combined impacts of the heat wave and of the heavy precipitation on the firn layer, we applied the physics-based, multilayer, detailed firn model SNOWPACK (Lehning et al. 2002b,a), with recent modifications for application to the polar ice sheets (Keenan et al. 2021; Wever et al. 2022) to investigate the impact of the heat wave on the surface energy balance and the near-surface firn layers. SNOWPACK calculates, among other properties, firn density, microstructure, and water percolation. Densification of the surface layers explicitly takes into account compaction during drifting snow conditions. Typical layer resolution is on the order of 0.5–2 cm near the surface to 1 m at 100 m below the surface. As in previous studies using SNOWPACK for the firn layer (Keenan et al. 2021; Thompson-Munson et al. 2023), SNOWPACK was forced by the MERRA-2 atmospheric reanalysis precipitation, air temperature, relative humidity, wind speed, and incoming longwave and shortwave radiation (Gelaro et al. 2017), relying on the SNOWPACK-calculated snow surface temperature as well as the parameterized surface albedo (Groot Zwaaftink et al. 2013) to calculate net shortwave and longwave radiation. This allows SNOWPACK to consider the energy balance consistently with the state of the firn layer, for example regarding the skin temperature, as well as the heat advection within the firn near the surface. We ran SNOWPACK for the Antarctic Ice Sheet on the MERRA-2 grid, but to reduce computational cost, neighboring grid cells with very similar climatology were grouped (Smith et al. 2020). Spinup of the firn column was achieved by repeating the 1980–2021 period until 150-m-deep firn was reached, or the bottom 3 m consisted of solid ice. We then ran until 31 March 2022, after which we extracted the energy balance components (discussed in Part I), density, and firn air content between 0000 UTC 14 and 0000 UTC 19 March. Based on the standard deviation determined over the 42 years between 1980 and 2021 over these exact 5 days, we calculated standard scores, or Z scores, denoting how many standard deviations the 2022 value deviated from the 1980 to 2021 mean.

d. Satellite observations of Conger Ice Shelf and sea ice

We analyzed available satellite imagery to characterize the style and timing of the breakup of the Conger Ice Shelf. *Landsat-7* and *-8* data provided the primary means to document the progressive retreat of the ice shelf over the last ~20 years. *Sentinel-1* radar images were used to assess conditions immediately preceding and following the ice shelf collapse. Likewise, MODIS images were assessed to further constrain the timing of ice shelf collapse.

Daily maps of sea ice concentration were obtained from the National Snow and Ice Data Center. From these, the change in sea ice extent after the passage of the AR was calculated. Landfast sea ice (fast ice) was manually mapped from composite cloud-free NASA moderate-resolution imaging spectroradiometer (MODIS) imagery following Fraser et al. (2020).

e. Cosmic ray measurements at Concordia Station

In addition to the measurements described above, we used measurements of neutron spectra made at Concordia Station since December 2015 (Hubert 2016) as part of the Continuous High-altitude Investigation of the Neutron Spectra for Terrestrial Radiation Antarctic Project (CHINSTRAP), supported by the French Polar Agency (IPEV). The neutron spectrometer records the neutron spectrum from the thermal region up to the GeV energy range, using multisphere spherical 3He proportional counters placed in spherical moderators with different diameters and consisting of high-density polyethylene and metallic shells (Cheminet et al. 2012; Hubert et al. 2019). The interaction of cosmic rays with liquid and vapor water content was analyzed using liquid water paths measured by a radiometer operated at Concordia Station in the framework of the HAMSTRAD project (Ricaud et al. 2010).

f. Snow temperature and isotope measurements/modeling at Concordia station

Snow temperature measurements recorded hourly at Concordia with 32 Pt100 sensors were used. The sensors were distributed every 5–10 cm in the first meter and then progressively more sparsely down to depths of 13 m. The accuracy is better than 0°C according to in-laboratory calibration (note, however, that the upper sensor may be subject to solar heating). The relative distance between the sensors is known with subcentimeter precision (enforced by a rigid support) but the position of the sensor relative to the surface is only measured once a year and is subject to centimeter-scale changes between measurements.

Vapor isotopic composition measurements were made at Concordia Station, as a surrogate for precipitation isotopic composition, in order to evaluate the imprint of the warm anomaly. Indeed, at first order, the vapor isotopic composition shares variability with the isotopic composition of the local precipitation (Leroy-Dos Santos et al. 2020). Continuous measurements of the water vapor isotopic composition were performed with a Picarro analyzer (L2130-i), similarly to Casado et al. (2016) and Leroy-Dos Santos et al. (2021). The raw data provided by the instrument were then corrected for the humidity response of the instrument and calibrated against the Vienna Standard Mean Ocean Water (VSMOW) scale to get absolute values [calibration protocol described in Leroy-Dos Santos et al. (2021)]. Typically, these measurements are only used in summer (humidity above 200 ppmv) due to the challenge of interpretation in winter, when humidity is extremely low (often below 50 ppmv). However, during the AR, humidities up to 3000 ppmv were observed, enabling us to have an unbiased picture of the isotopic composition anomaly induced by the event.

We combined the vapor monitoring with a virtual firn core model to document how the atmospheric monitoring applies to ice cores. The virtual firn core generator simulates the signal recorded of the isotopic composition in the snow (Casado et al. 2020). For each precipitation event, a layer of snow is added to the simulation of the firn formed before, with a thickness determined by the precipitation amount and an isotopic composition determined by the temperature, assuming a linear relationship (Stenni et al. 2017), where both precipitation amount and temperature are determined from ERA5. Since the precipitation amount varies, the layers are irregular. The vertical profile was then resampled onto a regular, millimetric-resolution scale before applying diffusion using a simulated density (Herron and Langway 1980) and a classical isotopic diffusion scheme (Gkinis et al. 2014). Finally, the firn core block average was computed at a resolution of 1 cm, similarly to what can be sampled in an ice core.

Table S1 in the online supplemental material summarizes type and purpose of reanalysis, model, and instrumental data utilized in this study. See Fig. 1 in Part I for a map showing station locations.

3. Ice sheet impacts

a. Surface mass balance impacts

Precipitation over the ice sheet and ice shelves was investigated using MAR regional climate model as well as global reanalysis products. The March transition to winter meant that most of the AR precipitation across East Antarctica fell in the form of snow, resulting in an overall large net-positive surface mass balance (SMB) gain. The extent and intensity of the moisture transport resulted in an extreme precipitation event over portions of the interior East Antarctic polar desert (see Turner et al. 2019). Over the whole ice sheet, total precipitation in March 2022 was 306 Gt in MAR (43-Gt anomaly relative to 1980–2021), 298 Gt in ERA5 (43-Gt anomaly), and 326 Gt in MERRA-2 (54-Gt anomaly) (Figs. 1 and 2). The event accounted for 32% of the March 2022 ice sheet-integrated total precipitation and up to 90% of the March 2022 total precipitation in local areas of the East Antarctic Ice Sheet (MAR). MAR, ERA5, and MERRA-2 show similar March total values as well as totals specific to this event.

While the AR generated heavy snowfall across the East Antarctic Ice Sheet, rainfall during the event was located primarily over coastal East Antarctica. Although rain events over coastal stations in East Antarctica typically occur a couple of days per year during March (Vignon et al. 2021), this mid-March rainfall was notably intense. Over the whole ice sheet, there was 2.12 Gt of simulated rainfall in MAR during March 2022 (0.49-Gt anomaly relative to 1980–2021) (Fig. 1).

Such an unusual warm air intrusion over East Antarctica also led to surface melting in coastal East Antarctica. ARs are more often associated with surface melt along West Antarctica and the Antarctic Peninsula (Wille et al. 2022, 2019; Adusumilli et al. 2021), but do occasionally trigger melt in coastal Wilkes Land during summer months. However, observing modest melt during the winter transition season is much more unusual. MAR simulated 0.5 Gt of surface melt during the event, which is insignificant relative to the snowfall accumulation, but the occurrence of melt during the winter transition here is noteworthy. This melt occurrence was confirmed using spaceborne Advanced Microwave Scanning Radiometer for EOS (AMSR-E) and AMSR2 passive microwave radiometers applying a simple threshold algorithm (Torinesi et al. 2003; Picard and Fily 2006). The results show an exceptional situation for this time of the year, with up to 9 wet days in some locations and a maximal extent of 44 000 km^2 (Fig. S1 in the online supplemental material). This marks the most extensive melt

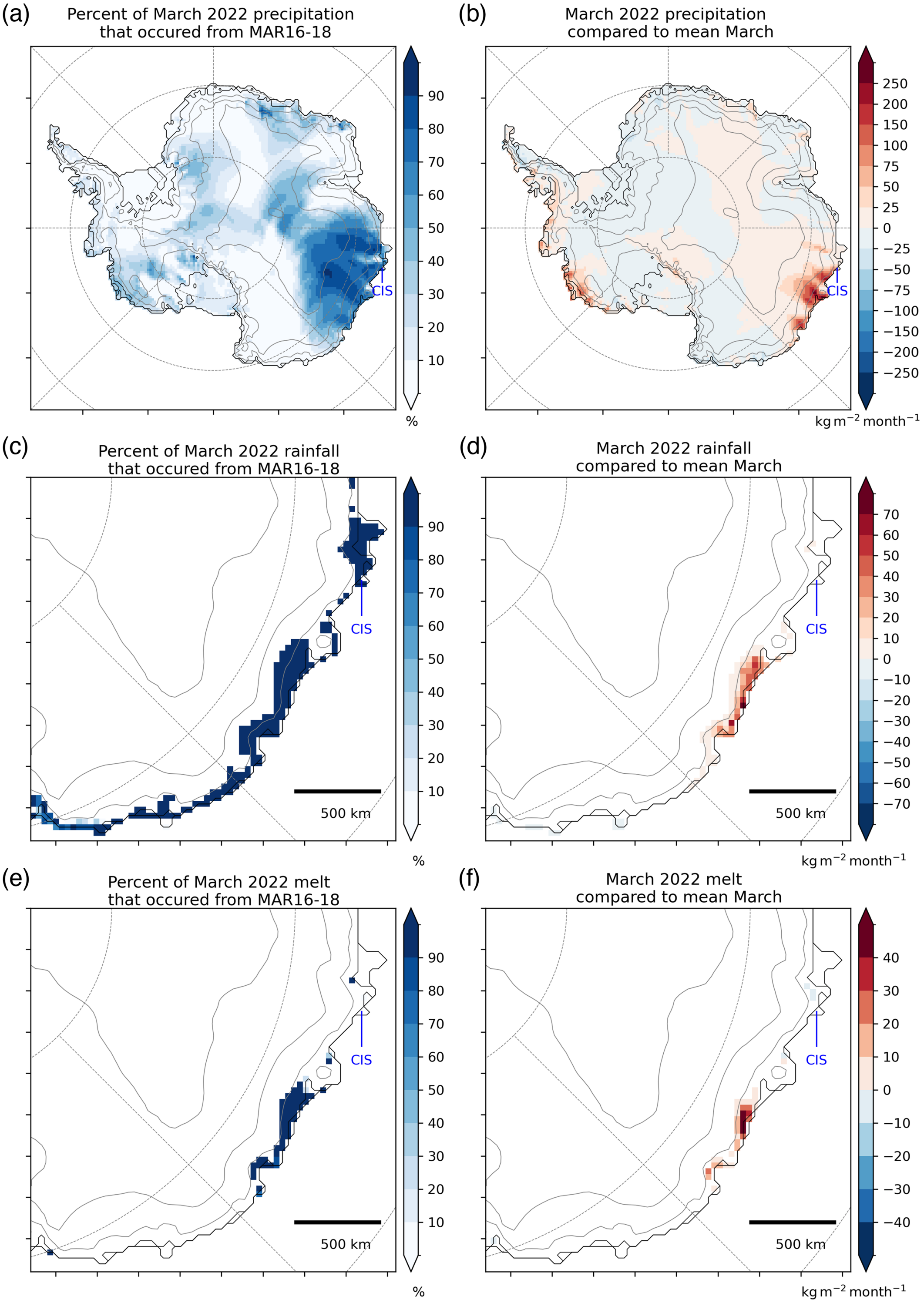

FIG. 1. The percent of total March (a) precipitation, (c) rainfall, and (e) melt that occurred between 16–18 Mar simulated by MAR. (b),(d),(f) The March monthly anomaly of the respective value with respect to the March mean from 1980 to 2021. CIS represents the location of the Conger Ice Shelf.

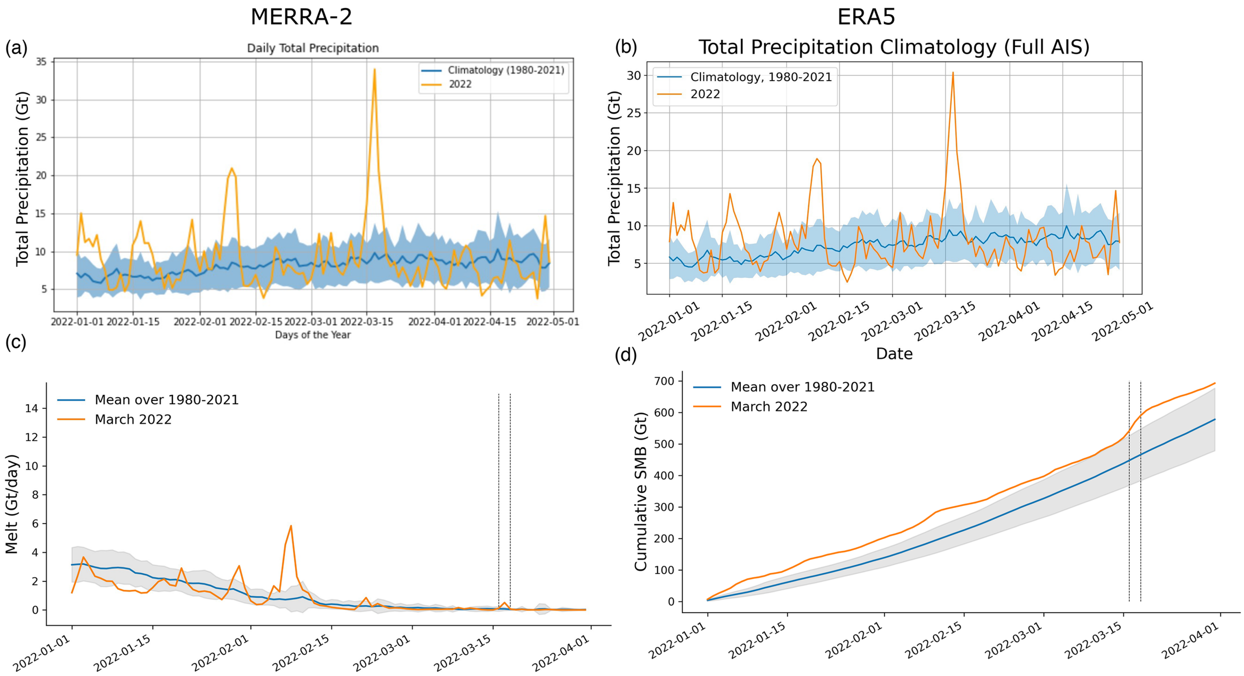

FIG. 2. Daily precipitation amounts across the Antarctic Ice Sheet from (a) MERRA-2 and (b) ERA5. (c) Daily surface melt and (d) annual cumulative surface mass balance changes from MAR for Wilkes Land, East Antarctica.

event recorded beyond 4 February in the Adélie and Wilkes region since satellite observational records began in 1979 (Datta et al. 2023).

The snow-to-rain transition is well visible in the measurements of the K-band MRR radar deployed at DDU. From 0700 to 1300 UTC 17 March, a sharp increase in Doppler velocity magnitude (up to 5 m s^{-1}) was noticeable between 1700 and 2100 m (Fig. 3a). This is a typical signature of the melting layer (Brast and Markmann 2020). Its altitude detected from the radar observations is consistent with the radiosoundings showing that temperatures were greater than 0°C up to 2100 m during the day of 17 March (Fig. 3b). A more detailed analysis of the precipitation event from the set of meteorological measurements at DDU is provided in the appendix.

b. Firn impacts

We used the SNOWPACK simulations to investigate how the combination of snowfall, local rainfall, high temperatures, and areas of surface melt impacted the near-surface firn structure on the ice sheet. When considering the total column firn air content (Fig. 4), we found an increase in the area affected by the heat wave, associated with the added firn air content by snowfall (Fig. 4a, along with Figs. S2a–c in the online supplemental material), particularly near the coast. The firn air content increase over large areas was 10–20 standard deviations above the climatological mean (Fig. 4b). To provide a characterization of the firn structure, we analyzed the surface density, defined as the density of the uppermost 10 cm of the firn (Fig. 5). We found that at the onset of the event, the density in the affected area was mostly within the ±2 standard deviations range in comparison with climatology (Figs. 5a,c). However, at the end of the event, an area could be identified with substantially higher density than the climatology (Figs. 5b,d). We found the strongest decrease in firn height from wind compaction (Figs. S2j–l), suggesting that wind erosion and deposition could have been a major driver in higher-than-normal surface density. Near Dome C, there was an area with above-normal settling rates (Figs. S2g–i), which could be attributed to warmer firn temperatures. Also near the coast, where melt occurred, higher-than-normal settling rates were found. Even though the impact of the higher density on, for example, SMB is likely limited, it may have an impact by a reduced potential for future erosion (thus, better locking in of the snowfall in the firn), but it is also something worthy of consideration when using repeat satellite altimetry to investigate the SMB impacts of such an event.

In contrast to the coast, in the interior of the East Antarctic Ice Sheet temperatures were not high enough for melt to occur. Nevertheless, increases in snow temperature had important impacts. Temperature measurements in the snow at Concordia Station (Fig. 6) showed a sharp increase from 15 March, with a maximum of −10.6°C reached at 500 UTC 18 March for the probe nearest the surface (estimated at depths of approximately 5 ± 5 cm). The penetration of this temperature pulse at depth is attenuated and lags in time due to the thermal diffusivity process. The maximum at 15 cm is −27°C, reached 4 h later and it is −42°C at 75 cm, reached 4 days later. A small maximum was still observed at 1.65-m depth 9 days later, but this maximum was close to the temperatures prevailing before the beginning of the event at that depth. Such rapid and strong change of temperature induced thermal gradients of >100°C m^{-1} near the surface. This, however, is not exceptional when compared with the gradients induced by the diurnal cycle of air temperature at Dome C.

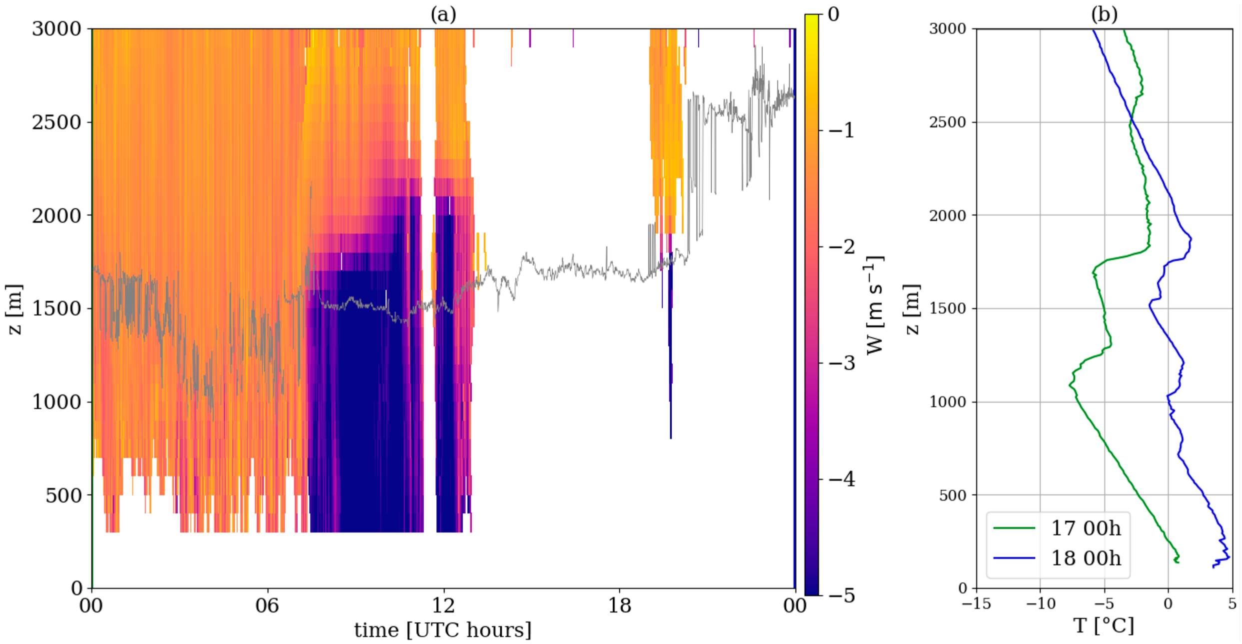

FIG. 3. (a) Time–height plot of the mean Doppler velocity (defined positive upward) at DDU on 17 Mar 2022. The thin gray line is the cloud base height detected by the ceilometer. White spaces correspond to periods during which the radar detects no precipitation signal. (b) Vertical profiles of temperature from the radiosoundings at 0000 UTC 17–18 Mar. Altitudes on the y axes are above ground level.

However, a bit deeper, at 30 cm, sustained gradients of >60°C m^{-1} were observed during a few days in March where the norm for the diurnal cycle-generated gradients is typically < 50°C m^{-1} even at summer solstice. The consequence of these combined high temperatures and strong thermal gradients was a strong transfer of vapor between snow layers, downward during the temperature rise and upward when the surface was cooling down. This led to marked snow metamorphism and likely contributed to the changes in isotope composition observed during this event.

4. Ice shelf and sea ice impacts

a. *Collapse of the Conger Ice Shelf*

In the midst of the heat wave in East Antarctica, the small Conger/Glenzer Ice Shelf (hereinafter Conger Ice Shelf) located near the AR landfall site in Wilkes Land collapsed (Fig. 7), thus raising questions about whether the two events were connected. Previous ARs have been connected to ice shelf collapses on the Antarctic Peninsula (Wille et al. 2022) but have not yet been linked to triggering ice shelf collapse

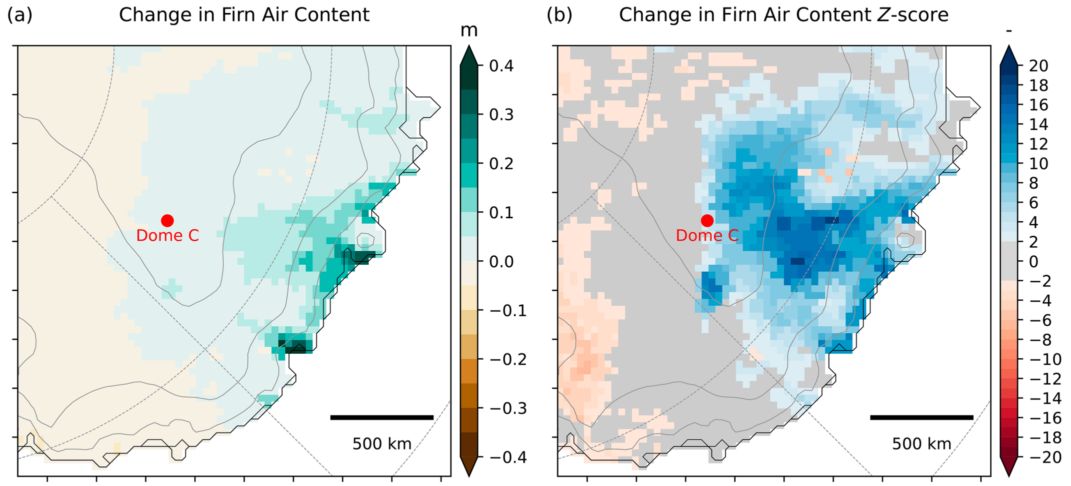

FIG. 4. (a) Change in firn air content over the period 14–19 Mar 2022, and (b) Z score of the changes in firn air content relative to the 14–19 Mar 1980–2021 climatology. Easting and northing are in the EPSG 3031 coordinate system (Antarctic polar stereographic projection).

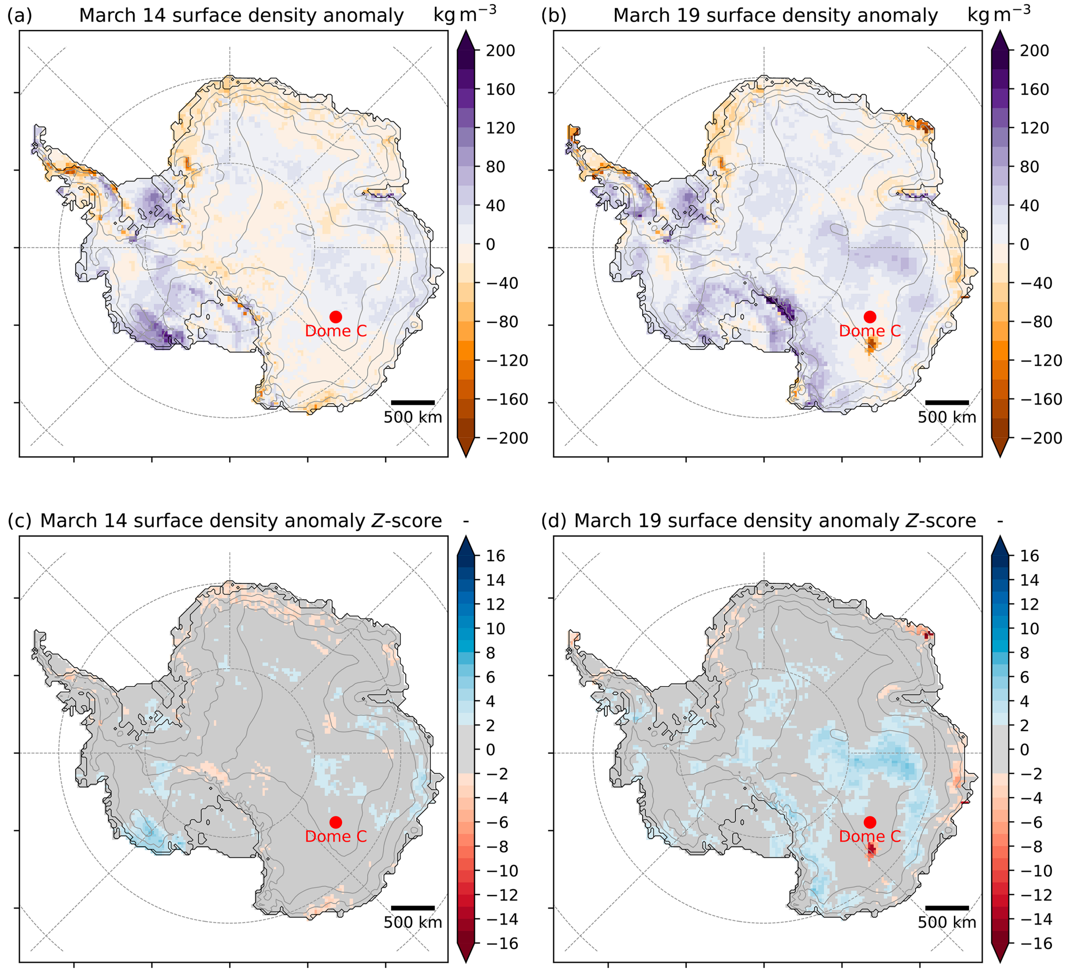

FIG. 5. Surface firn density anomaly at (a) the onset of the event on 14 Mar and (b) the end of the event on 19 Mar, and (c),(d) the associated *Z* scores. Surface density is defined as the density of the uppermost 0.1 m of the firn layer. Easting and northing are in the EPSG 3031 coordinate system (Antarctic polar stereographic projection).

in East Antarctica. ARs and their associated cyclones have been found to trigger calving events on the Amery Ice Shelf (Francis et al. 2021) and the Brunt Ice Shelf (Francis et al. 2022) where strong offshore winds generated by the cyclones induce oceanward sea slope, which acts dynamically on the ice shelf front leading to its calving.

In January 2022, the Conger Ice Shelf covered approximately 135 km^2, connecting ice draining from the Knox Coast of East Antarctica at ~103.5°E to an ~7-km-wide pinning point at the southern edge of Bowman Island (Fig. 7a). Over the preceding 20 years, the western ice margin of Conger Ice Shelf had progressively retreated, first losing contact with a smaller, unnamed island after 2011 and in subsequent years retreating farther to the east. This retreat left the Conger Ice Shelf in a structurally weakened state through the progressive loss of buttressing provided by the islands.

During January through early March 2022, the western margin of the ice shelf was bounded by open water, whereas the eastern margin terminated in a mélange of landfast sea ice (fast ice) and calved icebergs. On 5 March 2022, *Sentinel-1* radar imagery recorded a calving event at the southern (landward) margin of the ice shelf (Table 1). Within the next two days, the ice shelf calved a series of icebergs including iceberg C-37 at its northern extent, causing loss of contact with its pinning point on Bowman Island (Fig. 7b). Subsequent imagery on 12 March 2022 shows the resulting icebergs being swept westward with the main trunk of Conger Ice Shelf and landfast sea ice to the east still intact. MODIS imagery from 14 March shows the shelf still intact. Two days later on 16 March 2022, MODIS imagery showed that the entire Conger Ice Shelf had collapsed, producing iceberg C-38, and releasing a large portion of the landfast sea ice to east of the former shelf. Given available data, we expect that final collapse of the Conger Ice Shelf was underway by 15 March 2022 (Table 1). By 19 March 2022 (Fig. 7d), this ice had mostly been swept westward, leaving a broken mélange of ice and open water in the place where the former ice shelf resided.

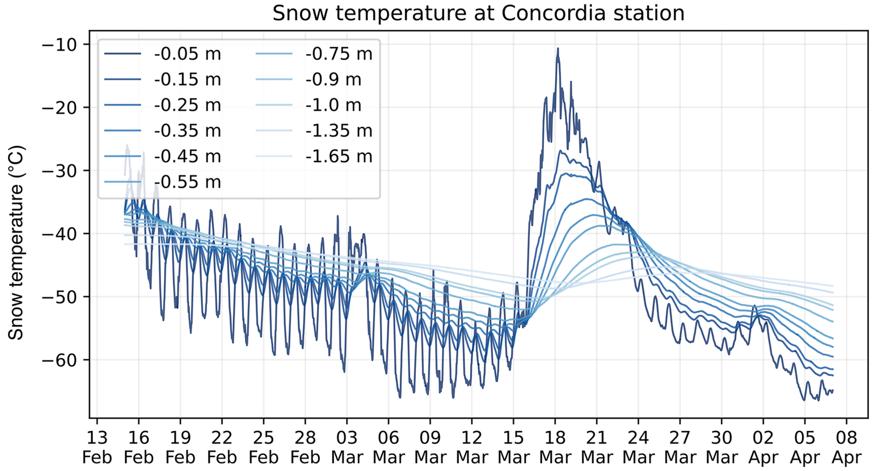

FIG. 6. Hourly snow temperature measurements at Concordia Station using Pt100 sensors.

In the weeks before the ice shelf collapsed, radar backscatter measurements from *Sentinel-1* did not indicate any surface melting on the Conger Ice Shelf or the adjacent sea ice, suggesting collapse was not triggered by surface melt-induced hydrofracturing. Indeed, available *Sentinel-1* backscatter indicated surface melting occurring only after the collapse, likely indicating the presence of AR-associated heat at this site on or before 17 March. As such, the structural precursor for ice

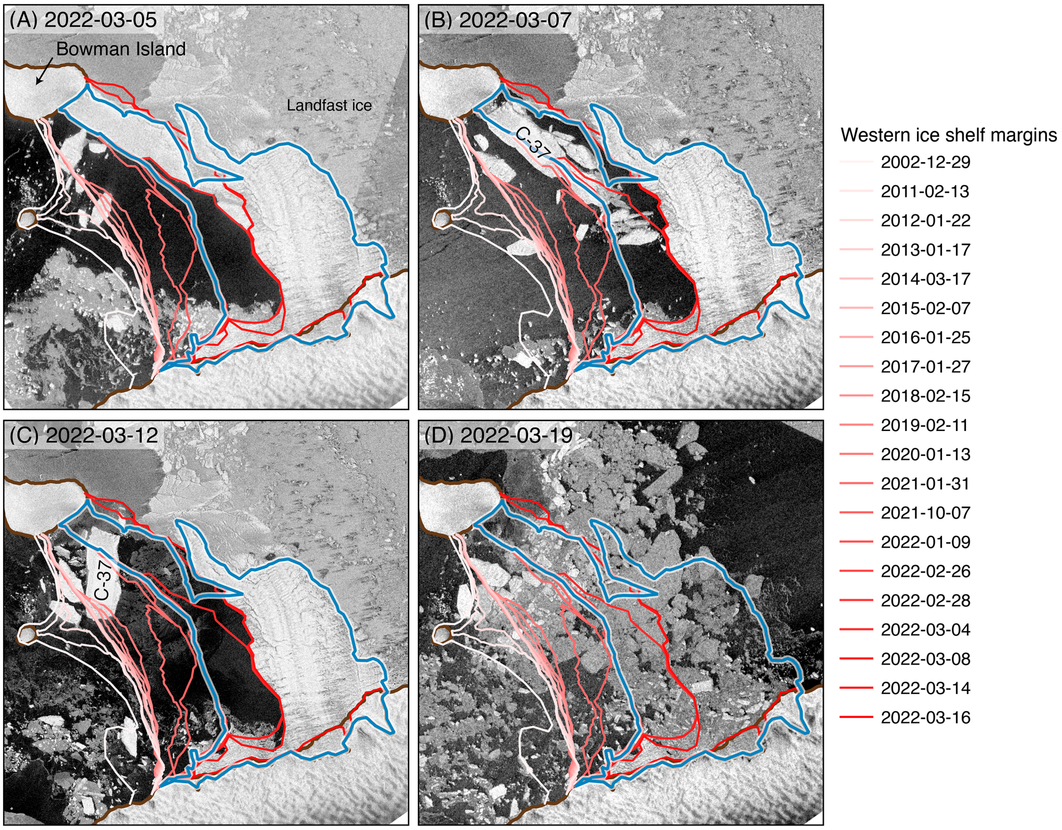

FIG. 7. Twenty years of progressive Conger Ice Shelf retreat followed by its abrupt and near-total collapse in March 2022 as seen in *Sentinel-1* radar imagery. Western ice shelf margins over 2002–22 were determined via Landsat imagery. The blue line indicates full ice shelf extent on 22 Feb 2022. The image dates are (a) 5, (b) 7, (c) 12, and (d) 19 Mar. The brown lines show coastlines and ice sheet grounding lines.

TABLE 1. Timeline of consequential events with regard to the Conger Ice Shelf.

Date	Status of fast ice/ice shelves
5 Mar 2022	Calving of southern portion of Glenzer Ice Shelf
7 Mar 2022	Remaining part of Glenzer Ice Shelf (abutting Bowman Island) calves
15 Mar 2022	AR landfall east of Shackleton Ice Shelf. Conger Ice Shelf, plus thick, 2200-km^2 fast ice breaks out (including thick, multiyear fast ice); eastern flank of fast ice remains
19 Mar 2022	End of AR event in this region
20 Mar 2022	Complete breakout of remaining fast ice east of Conger Ice Shelf
~26 Mar 2022	Fast ice reforms, composed of broken-out fast ice

shelf collapse appears to be the dual calving events at the southern margin on 5 March and two days later on 7 March during which the northern edge of the ice shelf became unpinned from Bowman Island. During this period, a stationary and intense cyclone occurred at the mouth of the ice shelf to the west of the AR landfall location (see Fig. 2b in Part I), driving strong anomalous surface winds. The AR on 15 March made landfall just east of the Conger Ice Shelf (see Fig. 4a in Part I).

Assessment of wave swell and wind data from ERA5 shows that conditions during these two calving events were not anomalous. However, ERA5 indicates highly anomalous wave swell and easterly winds on 14 March 2022 (Fig. 8), the day before the presumed ice shelf collapse [see Bruno et al. (2020) for assessment of ERA5 wave swells]. These data are also supported by observations on 14 March from Casey Station (~335 km east of Conger) that recorded 37 m s^{-1} easterly winds and at the Bunger Hills Station (~140 km southwest of Conger) where 19 m s^{-1} winds were recorded, despite being relatively sheltered by the plateau. These anomalous winds were again associated with the intense, stationary cyclone present to the west of the AR. The collapse appears to have been triggered by oceanward high sea surface slopes resulting from the strong offshore winds (e.g., Francis et al. 2022, 2021). As such, these highly anomalous easterly winds and the associated wave swell likely acted to dislodge the recently unbuttressed Conger Ice Shelf, leading to its abrupt

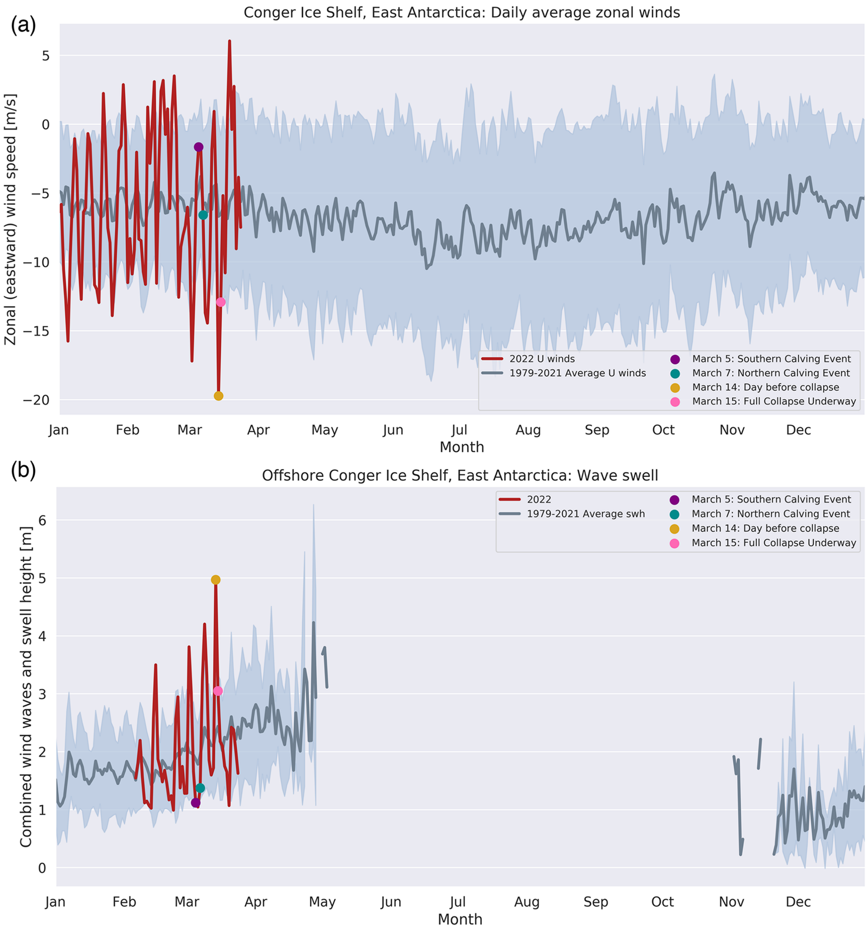

FIG. 8. (a) Zonal winds and (b) wave swell in the vicinity of Conger Ice Shelf in March 2022 as recorded by ERA5 reanalysis. The gray shading is ±1 standard deviation from the 1979–2021 mean.

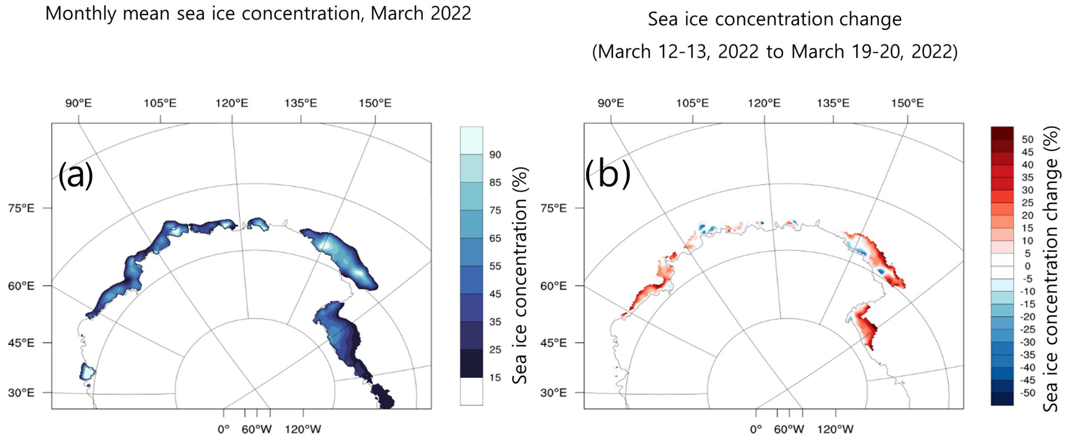

FIG. 9. (a) Sea ice concentration average for March 2022, and (b) sea ice concentration difference between pre- (12–13 Mar) and post- (19–20 Mar) AR event. Sea ice in (a) and (b) is only considered when the area has a March monthly concentration greater than 15%. Data are from the National Snow and Ice Data Center.

demise and the rapid westward advection of its remnants (Fig. S3 in the online supplemental material).

b. Sea ice effects

During late summer 2022, Antarctic wide sea ice extent was at a satellite-era record minimum, a record reached on 25 February 2022 (Turner et al. 2022a). This was notably evident around the Conger Ice Shelf, which was exposed to the open ocean at the time of its collapse, thus allowing swells to destabilize the ice shelf front (see Massom et al. 2018; Wille et al. 2022; Teder et al. 2022). For March 2022, sea ice concentration (SIC) was overall lower than normal years, especially in the Ross Sea where SIC was lower by more than 45% (Fig. 9). Turner et al. (2022b) attributed almost half of the signal of the satellite-era record low Antarctic sea ice extent in late February 2022 to strong offshore winds in October/November 2021 leading to increased sea ice loss. Victoria Land was within the footprint of the AR event (see Fig. 4 in Part I) while high temperature anomalies extended across Victoria Land and the western Ross Sea (see Fig. 3 in Part I). After the AR event from 14 to 18 March, sea ice overall increased off the Victoria Land and the Ross Sea. When we eliminate climatological fluctuations, the SIC appears to have increased in the same locations but decreased slightly outside the Ross Sea.

For the region of East Antarctica between the Amery Ice Shelf and the Ross Sea (72° to 180°E), fast-ice extent prior to the landfall of the AR (2 to 16 March) was already at the lowest on record, at ~56 000 km^2 (as shown in Fig. 10a; i.e., approximately 46 000 km^2 below the baseline extent for this time of year; Fraser et al. 2020, 2021, 2022). This further declined following the passage of the AR (17 to 31 March) to ~51 000 km^2 (i.e., less than half of the climatological average for this region at this time of year; ~109 000 km^2). The loss of fast ice between these two time periods occurred largely around the Conger Ice Shelf, as indicated in Fig. 10b. Much of this lost fast ice was generally multiyear, and broke out only infrequently (since 2000, only 2011, 2012, 2014 and 2020 saw near-complete breakouts). In the future, fast ice is less likely to remain throughout the summer without the mechanical support of the Conger Ice Shelf (Fraser et al. 2023).

The effects of the AR-associated event were furthermore exerted on fast ice beyond the Conger Ice Shelf vicinity. Normally fast ice formation begins during March in the McMurdo Sound in the Ross Sea region; however, in 2022 the fast ice stabilization ("freeze-up") in the Sound was significantly delayed (C. Kircher, Scott Base Winter Field Support 2021/22, Antarctica New Zealand, 2022, personal communication). As shown by Fig. S4 in the online supplemental material, the mean 2-m temperature on 18 March was elevated in a region outside the broken temperature hatched area, including Ross Island and McMurdo Sound (see Fig. 1 in Part I). Figure S4 also shows enhanced near-surface temperatures for Ross Island and McMurdo Sound for the period 14–20 March 2022. However, those temperatures were still cold enough for sea ice formation to occur, and the ocean would already have been at the freezing point temperature. The more important factor for fast ice formation and possible freeze-up in McMurdo Sound is the wind strength and direction. Figure S4 illustrates that maximum wind speeds were southwesterlies (i.e., offshore winds) that reached 17 m s^{-1} at 0400 UTC 16 March and 17.6 m s^{-1} at 1400 UTC 16 March. Further research is required to determine if the AR-associated event preconditioned McMurdo Sound for low extent throughout the winter.

5. Influences on markers for past climate reconstruction

a. Impacts of atmospheric moisture on cosmic rays

One unexpected observation during the AR event was the novel observation of a discernible impact of large atmospheric water content on cosmic ray measurements at Concordia Station. For context, the primary cosmic rays (CRs) interact with atmospheric atoms, producing secondary particles such as neutrons, protons, muons, pions, or electrons (Grieder 2001). In the lower atmosphere and ground, secondary CRs properties can be impacted by the short-term primary CRs changes (magnetic solar event and solar flare). Secondary cosmic-ray-

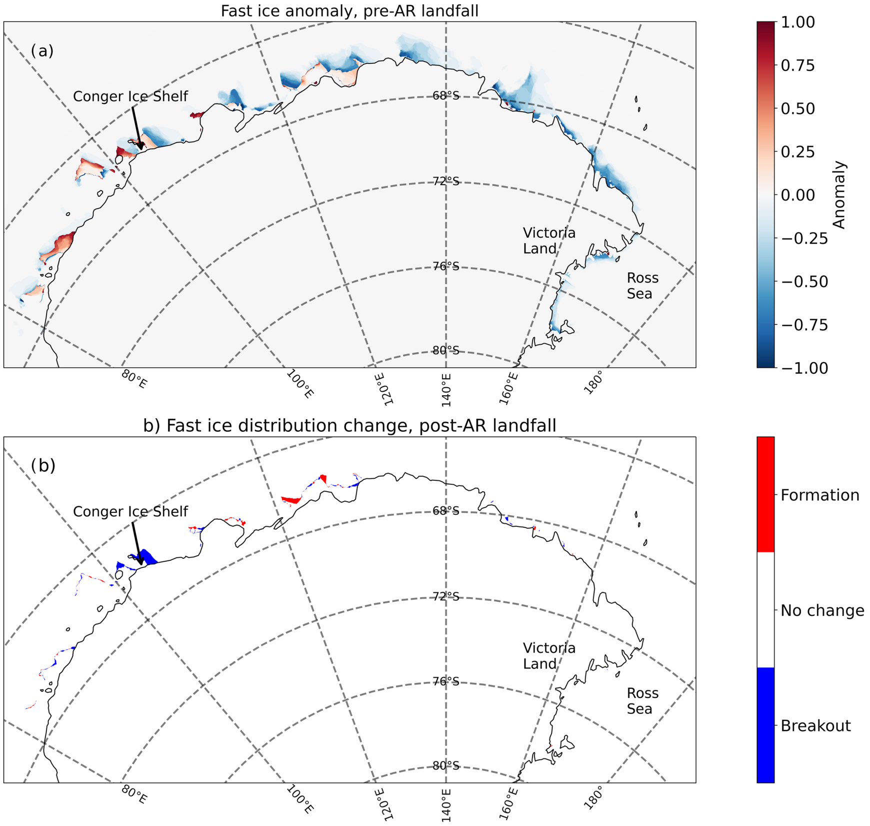

FIG. 10. (a) Fast ice anomaly distribution for early-to-mid-March 2022 (day-of-year range 61–75). The anomaly distribution was calculated by subtracting the long-term mean fast ice coverage [2000–18; from Fraser et al. (2020)] in early-to-mid March from the early-to-mid March 2022 observations. (b) Change in fast ice between early-to-mid March 2022 (pre-AR landfall) and late March–early April 2022 (post-AR landfall; day-of-year range 76–90). The distribution change map was calculated as the difference between these two maps (day-of-year 76–90 minus day-of-year 61–75). "Formation" indicates ice present in the day-of-year 76–90 map but not present in the earlier map (and vice versa for "breakout").

induced-neutrons are influenced by environmental and systematic effects, in particular the atmospheric pressure, the hydrometric environment close to the instrument (snowfall), and the atmospheric water vapor. Another influence concerns the albedo neutron produced by the interaction of air-shower neutrons with the soil. Hydrogen in soil, air, and snow determines the amount of ground albedo neutrons in the sensitive energy range from 1 to 10 MeV.

The transport of neutrons through matter (atmosphere, soil, ice, etc.) is profoundly influenced by the presence of hydrogen, in the form of vapor, liquid and solid water. Hydrogen is uniquely effective in moderating (slowing) neutrons by virtue of its low mass and relatively large elastic scattering cross section, which is a measure of the probability of interacting elastically with a neutron. Elastic collisions with hydrogen and other light nuclei progressively moderate a fast neutron until it is either absorbed by a nucleus or is reduced to a velocity on the order of the thermal motions of surrounding molecules, at which point there is no net change in energy through subsequent collisions.

Figure 11 presents the uncorrected and corrected total neutron fluxes, and the integrated water vapor and liquid water path (IWV and LWP, respectively; kg m^{-2}) during the period from 1 to 31 March 2022. The IWV and LWP (liquid water path) parameters were extracted from a radiometer operated in the framework of the HAMSTRAD project (Ricaud et al. 2010). Corrections applied to the uncorrected flux take into account influences of atmospheric pressure and the water vapor content (Hubert et al. 2019; Rosolem et al. 2013). A magnetic solar event impacted cosmic ray data on 14–15 March, without disturbing data during the AR. The neutron flux initially decreases on 13–14 March because of a solar magnetic event. Following a brief stabilization, a second decrease in cosmic ray intensity (~15%) was observed from 15 March, associated with the onset of the AR event (i.e., the liquid water in median/high altitude). The minimum in neutron flux was correlated with the IWV and LWP peaks. A recovery phase occurred, and the neutron flux trended toward its pre-event level with the meteorological conditions (IWV, LWP) returning to their baseline. Results show the importance of neutron

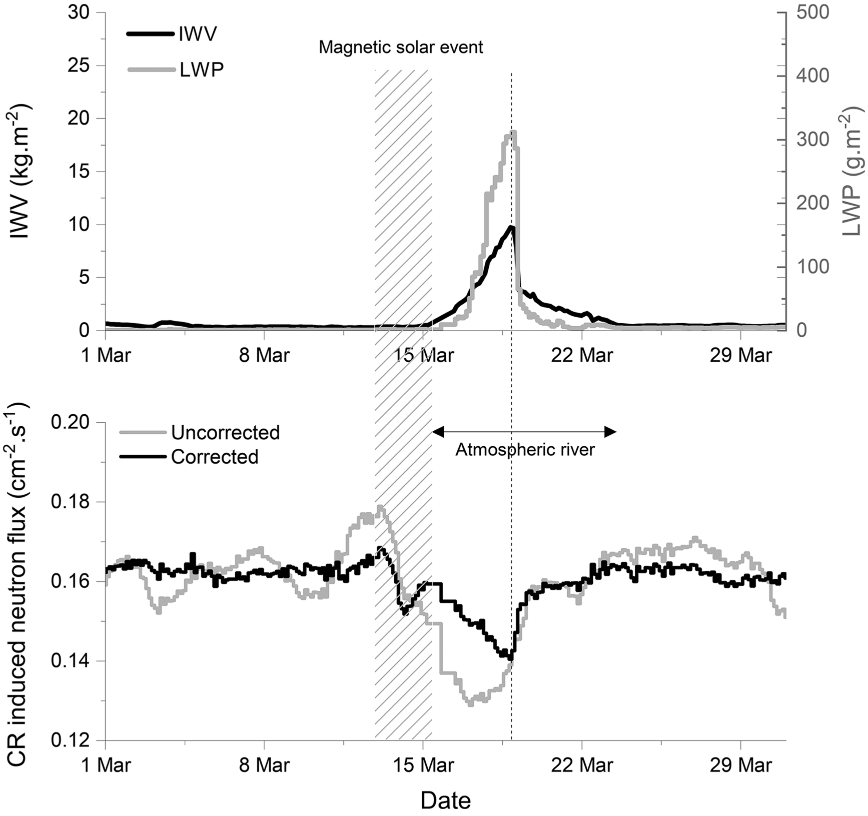

FIG. 11. (top) Integrated water vapor (kg m^{-2}; left axis) and liquid water path (g m^{-2}; right axis) during March 2022. (bottom) Uncorrected and corrected neutron flux (cm^{-2} s^{-1}) during March 2022. Corrections applied to the uncorrected flux take into account influences of atmospheric pressure and the water vapor content.

attenuation during particle transport mechanisms in a highly saturated atmosphere. Monte Carlo simulations based on nuclear transport of primary cosmic rays in the atmosphere (e.g., Geant4 or MCNPx tools) allow for studying physical mechanisms, to identify impact of liquid/vapor water on cosmic ray properties, then to determine physical parameters characterizing ARs (hydrogen quantity, dynamics, etc.).

Considering the special environmental condition of the Concordia Station (invariance of the neutron albedo, dry environment), this is the first time that attenuation caused by atmospheric liquid water has been observed. The CRs measurements on the Antarctic high plateau constitute a new opportunity to investigate rare meteorological events such as ARs. Cosmic ray activity leaves a beryllium-10 (B10) signature on the snow surface, which is used in ice-core dating. A discernable AR influence on B10 measurements could potentially lead the way to past climate water vapor reconstructions.

b. *Past climate reconstruction impacts*

The relatively warm and moist air mass responsible for the widespread snowfall led to profound changes in isotope anomaly measurements with implications for past climate reconstructions. Typical summer maximum values of humidity at Dome C are around 1000 ppmv, yet during this AR mixing ratios of almost 3000 ppmv were observed (Fig. 12a), underscoring the intensity of this event in comparison with the typical seasonal cycle. When compared with the levels measured in the beginning of March, the event translates into a vapor isotopic composition anomaly of roughly +28‰ for δ^{18}O above the pre-event baseline (Fig. 12b) and +229‰ for δD (same evolution over time as δ^{18}O; not shown here); both are greater than 10 sigma (std dev). The anomaly of d-excess is roughly +10‰ (Fig. 12c; <2 sigma). These observations do not reproduce the strong decrease of vapor d-excess isotopic composition observed in the Arctic at the North Greenland Eemian Ice Drilling site (NEEM; 77.45°N, 51.06°W) during an AR in 2012 (Bonne et al. 2015). Considering the low precision for the d-excess measurement here, it is unclear if the results contradict Bonne et al. (2015), or if the uncertainties of the measurement are hiding the feature.

Given the limited observational records across East Antarctica, past climate reconstructions and ensemble model simulations can provide context to the heat wave and its associated impacts on surface mass balance. The δ^{18}O anomalies could lead to a tremendous signal in ice cores, but it is not clear if such a short signal will be archived in the ice core isotopic composition. To evaluate the impact of the AR in the isotopic signal recorded by an ice core record, we made use of the

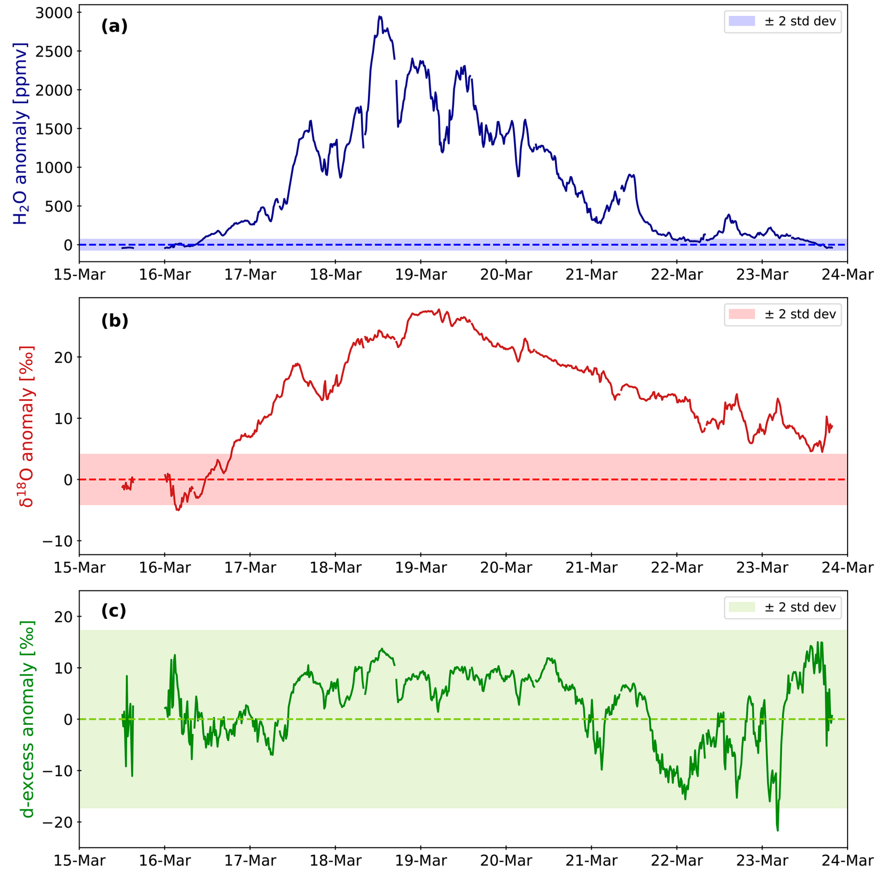

FIG. 12. Anomaly in (a) H_2O, (b) $\delta^{18}O$, and (c) d-excess during the atmospheric river event recorded at Dome C. The data presented correspond to the corrected and calibrated data averaged over 15 min. The data were then filtered with a 50-ppmv threshold on humidity (limit of instrument detection). The anomaly was calculated from a baseline corresponding to the mean values before the event (when there were reliable data: from 1 to 9 Mar 2022, represented by the dotted line at zero), and the shaded areas correspond to ±2 standard deviations.

virtual firn core generator [see section 2 herein and Casado et al. (2020)] and evaluated the isotopic anomaly imprinted during the event. We observed irregular seasonal cycles in which summer maximum values (dark red) vary a lot from one year to the next, while winter minimum values (blue) are relatively similar (Fig. 13a). During some winters, some warm events were visible during which the isotopic composition could be as high as during summer. The AR event we are studying here (marked with an orange diamond) is the only midseason (fall/spring) warm event, and the only nonsummer event during which values above −45‰ are visible. As such, it is almost 4‰ higher than the previous summer isotopic maximum. This suggests that the anomaly associated with this event should be imprinted in ice cores with high enough resolution both from this event and likely events in the past or future (see Casado et al. 2020) and for which the impact of stratigraphic noise is mitigated (Fisher et al. 1985; Münch and Laepple 2018).

We also evaluated over which time scale this signal could still be detected by comparing the isotopic anomaly between the virtual firn core with the AR imprinted, and a virtual firn core during which the precipitation amount during the event has been set to 0 (virtually preventing the event to leave any imprint on the isotopic composition). The preservation of the signature of this event depends mainly on the resolution of the sampling (diffusion has a negligible effect here). With a sampling corresponding to the monthly scale, the imprint of the event (4‰) is of the same order of magnitude as the signature of the previous summer period (Fig. 13b). For increasing sample length, an anomaly between 1.5‰ and 2‰ is imprinted for a sampling resolution lower than 2 years. Above this 2-yr threshold for the sampling resolution, the anomaly is diluted and decreases rapidly to drop below the detection limit for sampling interval corresponding to a 5–10-yr period (Fig. 13c). For the interpretation of the isotopic signal in ice core records, this extreme event of only several days can lead to a significant local positive anomaly over the equivalent of several years of snow accumulation. Taking into account the local temperature-to-isotope relationship (0.46‰ °C^{-1}: Stenni et al. 2016), it would create a positive bias on the temperature reconstruction made from an ice core at Dome C of roughly

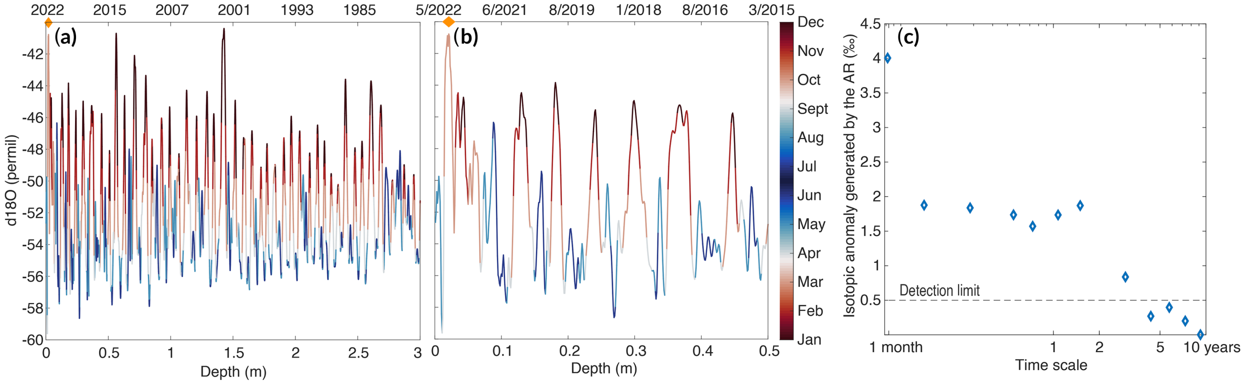

FIG. 13. Simulation of a virtual firn core at Dome C using ERA5 temperature and precipitation amount (a) starting from 1979 and (b) as a zoom over the most recent period (since March 2015). (c) Isotopic anomaly imprinted by the atmospheric river event in the virtual firn for samples of increasing thickness representing time scales ranging from 1 month to 10 years.

2°–3°C at a 2-yr resolution. Occurrences of such events can thus introduce important bias into the interpretation of the isotopic paleothermometer, in particular if the frequency of occurrence of these events changes for warmer or colder climatic conditions (see section 5 in Part I). This analysis relies on the accuracy of the reanalysis data used to feed the virtual firn core generator. ERA5 products are generally believed to model relatively well extreme events in extratropical regions (Lavers et al. 2022) and should be the most appropriate tool here to evaluate the impact of the March 2022 AR.

Few ice core records spanning more than recent decades have been drilled in the coastal region impacted by the AR in March 2022, meaning observations of regional snowfall accumulation variability are confined largely to satellite era estimates (Turner et al. 2019; Wille et al. 2021; Vance et al. 2016; Thomas et al. 2017). However, the Law Dome ice core on the Wilkes Coast preserves the longest and best studied annually resolved regional snowfall accumulation records with which to compare this event. Law Dome's high annual accumulation rate over the last two millennia has increased in recent decades from 0.67- to 0.75-m ice equivalent at the Dome Summit South drill site and has been related to the negative phase of the Southern Annular Mode (SAM; Marshall et al. 2017) and meridional circulation in the southern Indian Ocean with links to Pacific variability (Roberts et al. 2015; Jong et al. 2022; Crockart et al. 2021; Vance et al. 2022). Recent studies in this region have found a generalized pattern of northerly onshore moisture flow stemming from midlatitude lows interacting with downstream blocking highs leading to extreme precipitation events and temperature anomalies in the Wilkes Coast region (Wille et al. 2021; Pohl et al. 2021; Udy et al. 2022; Jackson et al. 2022). While this northerly moisture source is broadly analogous to the March 2022 synoptic pattern, the March 2022 event was clearly intensely impacted by interactions with low-latitude extreme events that led to the transport of heat and moisture well in excess of a "normal" extreme precipitation event in the Wilkes Coast region. This led to precipitation over a few days that is comparable to the annual mean accumulation for much of this region. Unfortunately, instrumentation failure at the Law Dome AWS prevented us from analyzing if surface melting may have occurred near the ice core drilling site.

6. Discussion and conclusions

a. *Summary of main results*

The historically intense AR/heat wave left a large footprint across a very large swath of the East Antarctic Ice Sheet that will be detectable in future paleoclimate records. Much of the surface warming was driven by a large radiative forcing sustained over several days as clouds laden with liquid water traversed deep into the Antarctic interior. Across the East Antarctic ice sheet, widespread rain and surface melt were observed along coastal regions, but the small mass losses were largely outweighed by high snowfall accumulation on the high plateau giving the event a largely net-positive SMB impact. High swells and intense surface winds generated by the extratropical cyclone associated with the AR helped trigger the final collapse of the already critically unstable Conger Ice Shelf while the storm further reduced sea ice and fast-ice extent, which were already at Antarctic-wide record minimums. The moisture advection associated with the AR had an unforeseen impact on cosmic ray measurements at Concordia Station with potential implications for past climate reconstruction. The relatively warm, humid airmass transported over East Antarctica caused δ^{18}O anomalies higher than the previous highest summer isotopic maximum with the ability to generate large positive temperature biases in past climate reconstruction from ice cores.

b. *Implications for long-term changes in Antarctic ARs and impacts*

The anthropogenic climate change signal could be arising in some regions of Antarctica, leading to intensified warming events. This is the case of the 2020 February record-breaking event in the Antarctic Peninsula, which was attributed to anthropogenic factors (González-Herrero et al. 2022) and was also caused by an Antarctic AR. The teleconnection with enhanced tropical convection in the SW Indian Ocean that spawned the eventual AR demands that we connect climate changes in the subtropics/midlatitudes to changes in extreme weather events over Antarctica. In a warmer world, the increased IVT, duration, and frequency of warmer air masses could play an important role in the intensification of these extreme events. This leads us to ask whether long-term changes in Antarctic climate extremes come from local changes over the continent or from remote changes farther from the continent. Tropical sea surface temperatures during this event, even under La Niña conditions, were warmer than they were 30 years ago (Hughes et al. 2018). These dynamics suggest that long-term changes in the nature of ARs may be a driver for these extreme events and thus there is a pressing need to better understand drivers of extreme events for a changing climate in Antarctica.

How these teleconnections change will influence our understanding of Antarctic ARs in a globally warmed world has implications for global sea level rise. If and when ARs become warmer and wetter, they will combine with basal melting to further destabilize ice sheets and shelves (Pritchard et al. 2012; Holland et al. 2015). ARs can affect mass balance by bringing both precipitation and heat toward the continent, both of which will increase in future warming scenarios (Espinoza et al. 2018; O'Brien et al. 2022). In the frozen interior of Antarctica, this precipitation will usually take the form of snowfall (adding mass), while at increasingly higher temperatures, especially at the margins, this precipitation can take the form of rainfall (Vignon et al. 2021). Both rainfall and surface melt reduce the albedo of the ice sheet surface (adding energy), initiating an ice–albedo feedback that enhances surface melt further. Additionally, even short-lived surface melt that refreezes can have long-term impacts on the characteristics of firn, by increasing density and even forming subsurface melt features. Over ice sheets, this can impact the path that meltwater takes toward the ice sheet edge, while over the ice shelves at the margins, these changes can lead to calving or even catastrophic hydrofracturing. While the loss of ice shelves (which also melt at the ice–ocean interface) does not immediately lead to sea level rise, the loss of their buttressing effect can accelerate the outflux of mass from the grounded ice sheet and increase sea level rise.

Although this AR event and associated temperature anomalies were extraordinarily higher than anything previously observed over Antarctica, the autumn occurrence and impact over the coldest part of the continent led to heavy snowfall and a highly net-positive SMB event. In fact, this event helped make 2022 a record-breaking snowfall year for the entire AIS that resulted in an overall mitigation of global sea level rise by around ~0.82 mm (Wang et al. 2023; Clem et al. 2023). However, if an AR of similar magnitude hypothetically occurred over the Thwaites Glacier region during peak summer, the results could potentially have been damaging for the glacial stability (Wille et al. 2019). Thus, if extreme events like what occurred in March 2022 happen more frequently in the future, it is important to determine whether they will be a net-positive for Antarctic SMB and act as a negative feedback for sea level rise or whether they will shift toward net-negative SMB events as is currently observed over Greenland (Mattingly et al. 2018, 2023).

Similarly for sea ice, this AR event's timing influenced its impacts, as it occurred soon after a satellite-era record minimum sea ice extent (25 February 2022: Turner et al. 2022a). This meant that the implications for sea ice were not as strong as if it had occurred at a different time. For example, heavy precipitation falling as snow on sea ice can slow sea ice formation by creating an insulating layer or increase sea ice formation through pushing down the sea ice surface causing flooding and through increasing the surface albedo, whereas rain on sea ice can melt snow cover affecting sea ice longevity (Maksym and Markus 2008; Fichefet and Maqueda 1999; Serreze and Meier 2019). It will be important in future research to examine effects on sea ice if AR extreme events become more frequent in the future and if similarly intense AR events precondition sea ice for prolonged low extent.

Overall, the AR associated with the March 2022 heat wave represents a massive anomaly in terms of moisture and heat transport in a climate system accustomed to large variability in temperature. This partially explains why this event is associated with the largest temperature anomaly ever recorded globally (Blanchard-Wrigglesworth et al. 2023) and helped make 2022 a net positive year for Antarctic mass balance (Datta et al. 2023; Wang et al. 2023). Properly understanding the variability of AR frequency, impacts, and intensity can help determine the possible range of impacts from future AR events. Such methodologies could help address the question of high-impact weather events (e.g., Marsigli et al. 2021), identified as a scientific priority by the World Meteorological Organization. Understanding and anticipating their effects is an issue of growing importance under a changing climate, and in the light of the compounding nature of some major events like the March 2022 AR in East Antarctica.

Acknowledgments. All authors particularly thank the national polar institutes such as the U.S. Antarctic Program, the French Polar Agency (IPEV), and the Australian Antarctic Division (AAD), without which none of the data used here would be available. Authors P. M. Rowe and X. Zou are grateful for funding from the NSF Office of Polar Programs under awards 2127632 and 2229392. Author R. T. Datta is grateful for funding from National Science Foundation (NSF) Office of Polar Programs award 1952199 and NASA award S000885. The PWRF model is developed and is maintained by the Polar Meteorology Group, Byrd Polar and Climate Research Center (BPCRC), The Ohio State University. PWRF simulations were performed on the San Diego Supercomputing Center's COMET resource through AR Program, Phase II 460001361 and III 4600014294 (State of California, Department of Water Resources). Authors J. D. Wille and V. Favier acknowledge support from the French Agence Nationale de la Recherche projects ANR-20-CE01-0013 (ARCA). Authors C. Amory and C. Kittel appreciate the computational resources provided by the Consortium des Équipements de Calcul Intensif (CÉCI), funded by the Fonds de la Recherche Scientifique de Belgique (F.R.S.–FNRS). Authors

M. A. Lazzara and D. Mikolajczyk are grateful for support from the NSF Office of Polar Programs under grants 1924730, 1951720, and 1951603. We also thank Bella Onsi for her assistance. This project received grant funding from the Australian government as part of the Antarctic Science Collaboration Initiative program. Authors I. J. Smith and G. H. Leonard were supported by grant MFP-UOO1825 from the Marsden Fund Council from government funding, administered by the Royal Society of New Zealand, and the Antarctic Science Platform (MBIE SSIF Programmes Investment contract ANTA1801). Author C. A. Shields was supported by U.S. Department of Energy, Office of Science, Office of Biological and Environmental Research (BER), Regional and Global Model Analysis (RGMA) component of the Earth and Environmental System Modeling Program, DE-SC0022070, NSF IA 1947282, and NCART NSF Cooperative Agreement 1852977. The National Center for Atmospheric Research is sponsored by the National Science Foundation. Author S. P. Alexander was supported by the Australian Antarctic Division's Australian Antarctic Science projects 4387 and 4637. We thank the Australian Bureau of Meteorology and the Australian Antarctic Division for providing the AWS data from the Australian Antarctic stations. Author S. González-Herrero was supported by the research group ANTALP (Antarctic, Arctic, Alpine Environments; 2017-SGR-1102) funded by the Agència de Gestió d'Ajuts Universitaris i de Recerca of the government of Catalonia. Authors S.-J. Kim and T. Choi were supported by the Korea Polar Research Institute (KOPRI) project "Understanding of Antarctic climate and environment and assessments of global influence" (PE23030) funded by the Ministry of Oceans and Fisheries. Author D. Udy was supported by an Australian Research Training scholarship and an Australian Research Council (ARC) Centre of Excellence for Climate Extremes top-up scholarship. Author T. Vance acknowledges support from the Australian Antarctic Program Partnership (ASCI000002). Udy and Vance also acknowledge support from ARC DP220100606. Author I. Ollivier was supported by the project DEEPICE. This project has received funding from the European Union's Horizon 2020 research and innovation programme under the Marie Skłodowska-Curie grant agreement 955750. Author L. D. Trusel acknowledges support from the NASA Cryospheric Sciences Program (Award 80NSSC20K0888). Author N. Wever was supported by the Swiss National Science Foundation (SNSF Grant 200020-179130). Author D. Bozkurt acknowledges support from ANID-FONDAP-1522A0001 and COPAS COASTAL ANID FB210021. Author I. V. Gorodetskaya expresses thanks for support by the strategic funding to CIIMAR (UIDB/04423/2020 and UIDP/04423/2020) and 2021.03140.CEECIND through national funds provided by the Fundação para a Ciência e a Tecnologia (FCT). Author R. D. Garreaud acknowledges support from ANID-FONDAP-1522A0001 and FONDECYT 1211412.

Data availability statement. We thank Météo France for launching daily radiosoundings at Dumont d'Urville station and for making the data freely accessible online (https://donneespubliques.meteofrance.fr/?fond=produit&id_produit=97&id_rubrique=33). MRR observations benefit from support by the French polar institute IPEV to project CALVA 1013. MRR and ceilometer data at Dumont d'Urville station are freely available upon request to author Christophe Genthon (christophe.genthon@cnrs.fr). We thank Claudio Durán-Alarcón for his help with the processing of the MRR data. We are grateful for the use of broadband radiation, radiosonde, and HAMSTRAD data over Dome C. Broadband radiation data are from the Institut national des sciences de l'Univers (INSU)/Centre National de la Recherche Scientifique (CNRS), the Institut polaire français Paul-Emile Victor (IPEV), Météo-France, and the Centre National d'Etudes Spatiales (CNES). The data for the atmospheric isotopic composition at Dome C in March 2023 are available upon request. These observations are made possible by the support from the French Polar Institute IPEV through the NIVO2 and ADELISE research programs.

APPENDIX

Further Analysis of Weather Conditions at Dumont d'Urville

Analysis of the coastal precipitation from remote sensing measurements and radiosoundings at DDU.

Figure A1 shows the evolution of the event from observations at DDU. On 15 March, the radar samples a period of virga with significant reflectivity in altitude but no signal near the ground (Fig. A1a). This situation is common at the beginning of precipitation events at DDU when snowfall sublimates in the dry boundary layer (see dotted purple line in Fig. A1c). The gradual decrease in the precipitating cloud base altitude corresponds to the transit of the warm front of the weather system above the station (Jullien et al. 2020).

At 0000 UTC 16 March the warm front moved to the south of DDU and moderate snowfall reached the ground. The radiosounding (red line, Figs. A1c–f) shows a well-marked warm layer between 1500 and 2500 m AGL that coincides with a northwesterly wind jet and likely corresponds to the warm conveyor belt. The latter advects a substantial amount of supercooled liquid water over the ice sheet as the air between 800 and 2500 m AGL is saturated with respect to liquid phase (solid red line in Fig. A1d).

Between 0700 and 1300 UTC 17 March, a sharp increase in reflectivity and Doppler velocity magnitude (up to 5 m s^{-1}) is noticeable between 1700 and 2100 m (Figs. A1a and A1b). This is a typical signature of a so-called melting layer (Brast and Markmann 2020) and DDU was therefore under the rain. Albeit infrequent, rainfall can occur at DDU in case of maritime intrusions favored by a blocking anticyclone (Vignon et al. 2021) as during the present event. While the near-surface temperature does not exceed 5°C, an ~2000-m height for the melting layer is surprising as a vertical extrapolation with a moist adiabatic gradient would give a 0°C level below 1000 m. The radiosounding of the 0000 UTC 18 March, that is, a few hours after the rain, exhibits temperatures > 0°C at almost all levels below 2000 m (blue line, Fig. A1c), and one can notice that the melting layer forms within a local elevated thermal

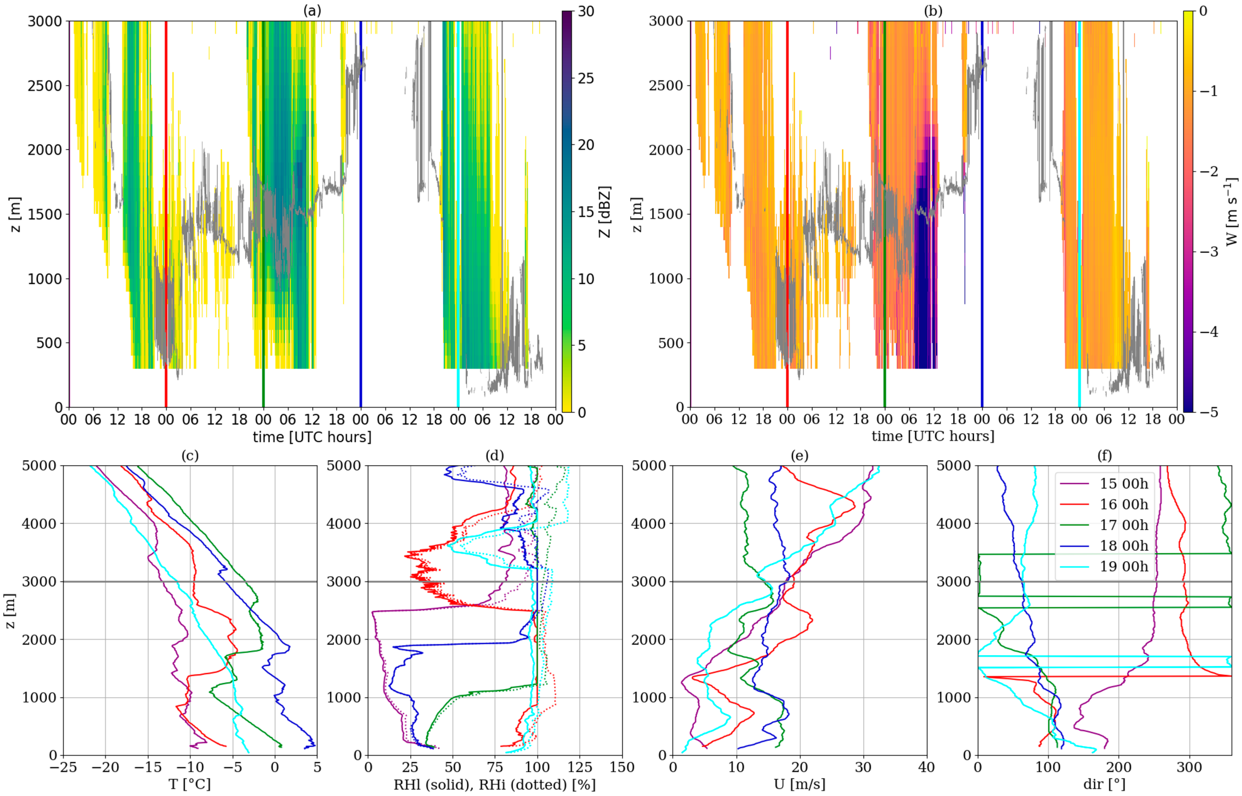

FIG. A1. Time–height plots of (a) the MRR reflectivity and (b) mean Doppler velocity (defined positive upward at DDU between 15 and 20 Mar. Vertical colored lines indicate the official time of the radiosoundings, but note that balloons are launched ~1 h earlier. The thin gray line is the cloud-base height detected by the ceilometer. Also shown are the vertical profiles of (c) temperature, (d) relative humidity, (e) wind speed, and (f) wind direction from radiosoundings. The horizontal gray line indicates the altitude of the highest radar gate. Altitudes on the *y* axes are above ground level.

inversion between 1700 and 2000 m (see blue line in Fig. A1c) with temperature above 0°C at the top. The thermal inversion is located below a jump in relative humidity (Fig. A1d) that corresponds to the base of the cloud whose height oscillates between 2000 and 2700 m around the sounding time in ceilometer measurements (see gray line in Figs. A1a and A1b). As the relative humidity in the cloud is saturated with respect to liquid water, the cloud is probably liquid or with a mixed-phase composition. Liquid-containing clouds being optically thick, the thermal inversion and the local temperature maximum > 0°C could be explained by the absorption of upwelling longwave radiation at cloud base. This process may be particularly intense in the present case as the surface temperature is warm and the air below the cloud very dry.

A third phase of precipitation (snowfall) is detected from 1900 UTC 18 to 1800 UTC 19 March. Using the reflectivity–snowfall relationship derived for DDU conditions in Grazioli et al. (2017) at the lowest radar gate, the total cumulative snowfall is equal to 9 mm w.e. over the 5 days (rainfall periods have been excluded). This is not a major contribution for the snow accumulation in the sector because the mean annual snowfall amount (estimated from MRR data at DDU over a 2-yr period) is about 780 mm w.e. (Jullien et al. 2020).

REFERENCES

Adusumilli, S., M. A. Fish, H. A. Fricker, and B. Medley, 2021: Atmospheric river precipitation contributed to rapid increases in surface height of the West Antarctic ice sheet in 2019. *Geophys. Res. Lett.*, **48**, e2020GL091076, https://doi.org/10.1029/2020GL091076.

Agosta, C., and Coauthors, 2019: Estimation of the Antarctic surface mass balance using the regional climate model MAR (1979–2015) and identification of dominant processes. *Cryosphere*, **13**, 281–296, https://doi.org/10.5194/tc-13-281-2019.

Blanchard-Wrigglesworth, E., T. Cox, Z. I. Espinosa, and A. Donohoe, 2023: The largest ever recorded heatwave—Characteristics and attribution of the Antarctic heatwave of March 2022. *Geophys. Res. Lett.*, **50**, e2023GL104910, https://doi.org/10.1029/2023GL104910.

Bonne, J.-L., and Coauthors, 2015: The summer 2012 Greenland heat wave: In situ and remote sensing observations of water vapor isotopic composition during an atmospheric river event. *J. Geophys. Res. Atmos.*, **120**, 2970–2989, https://doi.org/10.1002/2014JD022602.

Bozkurt, D., R. Rondanelli, J. C. Marín, and R. Garreaud, 2018: Foehn event triggered by an atmospheric river underlies record-setting temperature along continental Antarctica. *J. Geophys. Res. Atmos.*, **123**, 3871–3892, https://doi.org/10.1002/2017JD027796.

Brast, M., and P. Markmann, 2020: Detecting the melting layer with a micro rain radar using a neural network approach. *Atmos. Meas. Tech.*, **13**, 6645–6656, https://doi.org/10.5194/amt-13-6645-2020.

Bruno, M. F., M. G. Molfetta, V. Totaro, and M. Mossa, 2020: Performance assessment of ERA5 wave data in a swell dominated region. *J. Mar. Sci. Eng.*, **8**, 214, https://doi.org/10.3390/jmse8030214.

Casado, M., and Coauthors, 2016: Continuous measurements of isotopic composition of water vapour on the East Antarctic Plateau. *Atmos. Chem. Phys.*, **16**, 8521–8538, https://doi.org/10.5194/acp-16-8521-2016.

——, T. Münch, and T. Laepple, 2020: Climatic information archived in ice cores: Impact of intermittency and diffusion on the recorded isotopic signal in Antarctica. *Climate Past*, **16**, 1581–1598, https://doi.org/10.5194/cp-16-1581-2020.

Cheminet, A., V. Lacoste, G. Hubert, D. Boscher, D. Boyer, and J. Poupeney, 2012: Experimental measurements of the cosmic-ray induced neutron spectra at various mountain altitudes with HERMEIS. *IEEE Trans. Nucl. Sci.*, **59**, 1722–1730, https://doi.org/10.1109/TNS.2012.2201500.

Clem, K. R., and Coauthors, 2023: Antarctica and the Southern Ocean. *Bull. Amer. Meteor. Soc.*, **104**, S322–S365, https://doi.org/10.1175/BAMS-D-23-0077.1.

Crockart, C. K., and Coauthors, 2021: El Niño–Southern Oscillation signal in a new East Antarctic ice core, Mount Brown South. *Climate Past*, **17**, 1795–1818, https://doi.org/10.5194/cp-17-1795-2021.

Datta, R. T., J. D. Wille, D. Bozkurt, D. E. Mikolajczyk, K. R. Clem, Z. Yin, and M. Macferrin, 2023: Sidebar 6.1: The Antarctic heatwave of March 2022 [in “State of the Climate in 2022”]. *Bull. Amer. Meteor. Soc.*, **104**, S333–S335.

Djoumna, G., and D. M. Holland, 2021: Atmospheric rivers, warm air intrusions, and surface radiation balance in the Amundsen Sea embayment. *J. Geophys. Res. Atmos.*, **126**, e2020JD034119, https://doi.org/10.1029/2020JD034119.

Durán-Alarcón, C., B. Boudevillain, C. Genthon, J. Grazioli, N. Souverijns, N. P. M. van Lipzig, I. V. Gorodetskaya, and A. Berne, 2019: The vertical structure of precipitation at two stations in East Antarctica derived from micro rain radars. *Cryosphere*, **13**, 247–264, https://doi.org/10.5194/tc-13-247-2019.

Espinoza, V., D. E. Waliser, B. Guan, D. A. Lavers, and F. M. Ralph, 2018: Global analysis of climate change projection effects on atmospheric rivers. *Geophys. Res. Lett.*, **45**, 4299–4308, https://doi.org/10.1029/2017GL076968.

Fichefet, T., and M. A. M. Maqueda, 1999: Modelling the influence of snow accumulation and snow-ice formation on the seasonal cycle of the Antarctic sea-ice cover. *Climate Dyn.*, **15**, 251–268, https://doi.org/10.1007/s003820050280.

Fisher, D. A., N. Reeh, and H. B. Clausen, 1985: Stratigraphic noise in time series derived from ice cores. *Ann. Glaciol.*, **7**, 76–83, https://doi.org/10.3189/S0260305500005942.

Francis, D., K. S. Mattingly, S. Lhermitte, M. Temimi, and P. Heil, 2021: Atmospheric extremes caused high oceanward sea surface slope triggering the biggest calving event in more than 50 years at the Amery Ice Shelf. *Cryosphere*, **15**, 2147–2165, https://doi.org/10.5194/tc-15-2147-2021.

——, R. Fonseca, K. S. Mattingly, O. J. Marsh, S. Lhermitte, and C. Cherif, 2022: Atmospheric triggers of the brunt ice shelf calving in February 2021. *J. Geophys. Res. Atmos.*, **127**, e2021JD036424, https://doi.org/10.1029/2021JD036424.

Fraser, A. D., R. A. Massom, K. I. Ohshima, S. Willmes, P. J. Kappes, J. Cartwright, and R. Porter-Smith, 2020: High-resolution mapping of circum-Antarctic landfast sea ice distribution, 2000–2018. *Earth Syst. Sci. Data*, **12**, 2987–2999, https://doi.org/10.5194/essd-12-2987-2020.

——, and Coauthors, 2021: Eighteen-year record of circum-Antarctic landfast-sea-ice distribution allows detailed baseline characterisation and reveals trends and variability. *Cryosphere*, **15**, 5061–5077, https://doi.org/10.5194/tc-15-5061-2021.

——, and Coauthors, 2022: Antarctic landfast sea ice: Physical, biogeochemical and ecological significance. *Earth Space Sci. Open Arch.*, https://doi.org/10.1002/essoar.10512682.1, in press.

——, and Coauthors, 2023: Antarctic landfast sea ice: A review of its physics, biogeochemistry and ecology. *Rev. Geophys.*, **61**, e2022RG000770, https://doi.org/10.1029/2022RG000770.

Gehring, J., É. Vignon, A.-C. Billault-Roux, A. Ferrone, A. Protat, S. P. Alexander, and A. Berne, 2022: Orographic flow influence on precipitation during an atmospheric river event at Davis, Antarctica. *J. Geophys. Res. Atmos.*, **127**, e2021JD035210, https://doi.org/10.1029/2021JD035210.

Gelaro, R., and Coauthors, 2017: The Modern-Era Retrospective Analysis for Research and Applications, version 2 (MERRA-2). *J. Climate*, **30**, 5419–5454, https://doi.org/10.1175/JCLI-D-16-0758.1.

Gkinis, V., S. B. Simonsen, S. L. Buchardt, J. W. C. White, and B. M. Vinther, 2014: Water isotope diffusion rates from the NorthGRIP ice core for the last 16,000 years—Glaciological and paleoclimatic implications. *Earth Planet. Sci. Lett.*, **405**, 132–141, https://doi.org/10.1016/j.epsl.2014.08.022.

González-Herrero, S., D. Barriopedro, R. M. Trigo, J. A. López-Bustins, and M. Oliva, 2022: Climate warming amplified the 2020 record-breaking heatwave in the Antarctic Peninsula. *Commun. Earth Environ.*, **3**, 122, https://doi.org/10.1038/s43247-022-00450-5.

Gorodetskaya, I. V., M. Tsukernik, K. Claes, M. F. Ralph, W. D. Neff, and N. P. M. Van Lipzig, 2014: The role of atmospheric rivers in anomalous snow accumulation in East Antarctica. *Geophys. Res. Lett.*, **41**, 6199–6206, https://doi.org/10.1002/2014GL060881.

——, T. Silva, H. Schmithüsen, and N. Hirasawa, 2020: Atmospheric river signatures in radiosonde profiles and reanalyses at the Dronning Maud Land coast, East Antarctica. *Adv. Atmos. Sci.*, **37**, 455–476, https://doi.org/10.1007/s00376-020-9221-8.

Grazioli, J., J.-B. Madeleine, H. Gallée, R. M. Forbes, C. Genthon, G. Krinner, and A. Berne, 2017: Katabatic winds diminish precipitation contribution to the Antarctic ice mass balance. *Proc. Natl. Acad. Sci. USA*, **114**, 10 858–10 863, https://doi.org/10.1073/pnas.1707633114.

Grieder, P. K. F., 2001: Cosmic ray properties, relations and definitions. *Cosmic Rays at Earth*, P. K. F. Grieder, Ed., Elsevier, 1–53.

Groot Zwaaftink, C. D., A. Cagnati, A. Crepaz, C. Fierz, G. Macelloni, M. Valt, and M. Lehning, 2013: Event-driven deposition of snow on the Antarctic Plateau: Analyzing field measurements with SNOWPACK. *Cryosphere*, **7**, 333–347, https://doi.org/10.5194/tc-7-333-2013.

Herron, M. M., and C. C. Langway Jr., 1980: Firn densification: An empirical model. *J. Glaciol.*, **25**, 373–385, https://doi.org/10.3189/S0022143000015239.

Holland, P. R., and Coauthors, 2015: Oceanic and atmospheric forcing of Larsen C ice-shelf thinning. *Cryosphere*, **9**, 1005–1024, https://doi.org/10.5194/tc-9-1005-2015.

Hubert, G., 2016: Analyses of cosmic ray induced-neutron based on spectrometers operated simultaneously at mid-latitude and Antarctica high-altitude stations during quiet solar activity.

Astropart. Phys., **83**, 30–39, https://doi.org/10.1016/j.astropartphys.2016.07.002.

——, M. T. Pazianotto, C. A. Federico, and P. Ricaud, 2019: Analysis of the Forbush decreases and ground-level enhancement on September 2017 using neutron spectrometers operated in Antarctic and midlatitude stations. *J. Geophys. Res. Space Phys.*, **124**, 661–673, https://doi.org/10.1029/2018JA025834.

Hughes, T. P., and Coauthors, 2018: Spatial and temporal patterns of mass bleaching of corals in the Anthropocene. *Science*, **359**, 80–83, https://doi.org/10.1126/science.aan8048.

Jackson, S. L., T. R. Vance, C. Crockart, A. Moy, C. Plummer, and N. J. Abram, 2022: Climatology of the Mount Brown South ice core site in East Antarctica: Implications for the interpretation of a water isotope record. *Climate Past*, **19**, 1653–1675, https://doi.org/10.5194/cp-19-1653-2023.

Jong, L. M., and Coauthors, 2022: 2000 years of annual ice core data from Law Dome, East Antarctica. *Earth Syst. Sci. Data*, **14**, 3313–3328, https://doi.org/10.5194/essd-14-3313-2022.

Jullien, N., É. Vignon, M. Sprenger, F. Aemisegger, and A. Berne, 2020: Synoptic conditions and atmospheric moisture pathways associated with virga and precipitation over coastal Adélie Land in Antarctica. *Cryosphere*, **14**, 1685–1702, https://doi.org/10.5194/tc-14-1685-2020.

Keenan, E., N. Wever, M. Dattler, J. T. M. Lenaerts, B. Medley, P. Kuipers Munneke, and C. Reijmer, 2021: Physics-based SNOWPACK model improves representation of near-surface Antarctic snow and firn density. *Cryosphere*, **15**, 1065–1085, https://doi.org/10.5194/tc-15-1065-2021.

Kittel, C., and Coauthors, 2021: Diverging future surface mass balance between the Antarctic ice shelves and grounded ice sheet. *Cryosphere*, **15**, 1215–1236, https://doi.org/10.5194/tc-15-1215-2021.

Lavers, D. A., A. Simmons, F. Vamborg, and M. J. Rodwell, 2022: An evaluation of ERA5 precipitation for climate monitoring. *Quart. J. Roy. Meteor. Soc.*, **148**, 3152–3165, https://doi.org/10.1002/qj.4351.

Lehning, M., P. Bartelt, B. Brown, and C. Fierz, 2002a: A physical SNOWPACK model for the Swiss avalanche warning: Part III: Meteorological forcing, thin layer formation and evaluation. *Cold Reg. Sci. Technol.*, **35**, 169–184, https://doi.org/10.1016/S0165-232X(02)00072-1.

——, ——, ——, ——, and P. Satyawali, 2002b: A physical SNOWPACK model for the Swiss avalanche warning: Part II. Snow microstructure. *Cold Reg. Sci. Technol.*, **35**, 147–167, https://doi.org/10.1016/S0165-232X(02)00073-3.

Leroy-Dos Santos, C., and Coauthors, 2020: A 4.5 year-long record of Svalbard water vapor isotopic composition documents winter air mass origin. *J. Geophys. Res. Atmos.*, **125**, e2020JD032681, https://doi.org/10.1029/2020JD032681.

——, and Coauthors, 2021: A dedicated robust instrument for water vapor generation at low humidity for use with a laser water isotope analyzer in cold and dry polar regions. *Atmos. Meas. Tech.*, **14**, 2907–2918, https://doi.org/10.5194/amt-14-2907-2021.

Maahn, M., and P. Kollias, 2012: Improved micro rain radar snow measurements using Doppler spectra post-processing. *Atmos. Meas. Tech.*, **5**, 2661–2673, https://doi.org/10.5194/amt-5-2661-2012.

Maclennan, M. L., and Coauthors, 2022a: Climatology and surface impacts of atmospheric rivers on West Antarctica. *Cryosphere*, **17**, 865–881, https://doi.org/10.5194/tc-2022-101.

——, J. T. M. Lenaerts, C. Shields, and J. D. Wille, 2022b: Contribution of atmospheric rivers to Antarctic precipitation. *Geophys. Res. Lett.*, **49**, e2022GL100585, https://doi.org/10.1029/2022GL100585.

Maksym, T., and T. Markus, 2008: Antarctic sea ice thickness and snow-to-ice conversion from atmospheric reanalysis and passive microwave snow depth. *J. Geophys. Res.*, **113**, C02S12, https://doi.org/10.1029/2006JC004085.

Marshall, G. J., D. W. J. Thompson, and M. R. van den Broeke, 2017: The signature of Southern Hemisphere atmospheric circulation patterns in Antarctic precipitation. *Geophys. Res. Lett.*, **44**, 11 580–11 589, https://doi.org/10.1002/2017GL075998.

Marsigli, C., and Coauthors, 2021: Review article: Observations for high-impact weather and their use in verification. *Nat. Hazards Earth Syst. Sci.*, **21**, 1297–1312, https://doi.org/10.5194/nhess-21-1297-2021.

Massom, R. A., T. A. Scambos, L. G. Bennetts, P. Reid, V. A. Squire, and S. E. Stammerjohn, 2018: Antarctic ice shelf disintegration triggered by sea ice loss and ocean swell. *Nature*, **558**, 383–389, https://doi.org/10.1038/s41586-018-0212-1.

Mattingly, K. S., T. L. Mote, and X. Fettweis, 2018: Atmospheric river impacts on Greenland ice sheet surface mass balance. *J. Geophys. Res. Atmos.*, **123**, 8538–8560, https://doi.org/10.1029/2018JD028714.

——, J. V. Turton, J. D. Wille, B. Noël, X. Fettweis, Å. K. Rennermalm, and T. L. Mote, 2023: Increasing extreme melt in northeast Greenland linked to foehn winds and atmospheric rivers. *Nat. Commun.*, **14**, 1743, https://doi.org/10.1038/s41467-023-37434-8.

Mottram, R., and Coauthors, 2021: What is the surface mass balance of Antarctica? An intercomparison of regional climate model estimates. *Cryosphere*, **15**, 3751–3784, https://doi.org/10.5194/tc-15-3751-2021.

Münch, T., and T. Laepple, 2018: What climate signal is contained in decadal- to centennial-scale isotope variations from Antarctic ice cores? *Climate Past*, **14**, 2053–2070, https://doi.org/10.5194/cp-14-2053-2018.

O'Brien, T. A., and Coauthors, 2022: Increases in future AR count and size: Overview of the ARTMIP tier 2 CMIP5/6 experiment. *J. Geophys. Res. Atmos.*, **127**, e2021JD036013, https://doi.org/10.1029/2021JD036013.

Picard, G., and M. Fily, 2006: Surface melting observations in Antarctica by microwave radiometers: Correcting 26-year time series from changes in acquisition hours. *Remote Sens. Environ.*, **104**, 325–336, https://doi.org/10.1016/j.rse.2006.05.010.

Pohl, B., and Coauthors, 2021: Relationship between weather regimes and atmospheric rivers in East Antarctica. *J. Geophys. Res. Atmos.*, **126**, e2021JD035294, https://doi.org/10.1029/2021JD035294.

Pritchard, H. D., S. R. M. Ligtenberg, H. A. Fricker, D. G. Vaughan, M. R. van den Broeke, and L. Padman, 2012: Antarctic ice-sheet loss driven by basal melting of ice shelves. *Nature*, **484**, 502–505, https://doi.org/10.1038/nature10968.

Ralph, F. M., M. D. Dettinger, J. J. Rutz, and D. E. Waliser, 2020: *Atmospheric Rivers.* 1st ed. Springer, 252 pp.

Ricaud, P., B. Gabard, S. Derrien, J.-P. Chaboureau, T. Rose, A. Mombauer, and H. Czekala, 2010: HAMSTRAD-Tropo, a 183-GHz radiometer dedicated to sound tropospheric water vapor over Concordia Station, Antarctica. *IEEE Trans. Geosci. Remote Sens.*, **48**, 1365–1380, https://doi.org/10.1109/TGRS.2009.2029345.

Roberts, J., and Coauthors, 2015: A 2000-year annual record of snow accumulation rates for Law Dome, East Antarctica. *Climate Past*, **11**, 697–707, https://doi.org/10.5194/cp-11-697-2015.

Rosolem, R., W. J. Shuttleworth, M. Zreda, T. E. Franz, X. Zeng, and S. A. Kurc, 2013: The effect of atmospheric water vapor on neutron count in the cosmic-ray soil moisture observing system. *J. Hydrometeor.*, **14**, 1659–1671, https://doi.org/10.1175/JHM-D-12-0120.1.

Serreze, M. C., and W. N. Meier, 2019: The Arctic's sea ice cover: Trends, variability, predictability, and comparisons to the Antarctic. *Ann. N. Y. Acad. Sci.*, **1436**, 36–53, https://doi.org/10.1111/nyas.13856.

Smith, B., and Coauthors, 2020: Pervasive ice sheet mass loss reflects competing ocean and atmosphere processes. *Science*, **368**, 1239–1242, https://doi.org/10.1126/science.aaz5845.

Stenni, B., and Coauthors, 2016: Three-year monitoring of stable isotopes of precipitation at Concordia station, East Antarctica. *Cryosphere*, **10**, 2415–2428, https://doi.org/10.5194/tc-10-2415-2016.

——, and Coauthors, 2017: Antarctic climate variability on regional and continental scales over the last 2000 years. *Climate Past*, **13**, 1609–1634, https://doi.org/10.5194/cp-13-1609-2017.

Teder, N. J., L. G. Bennetts, P. A. Reid, and R. A. Massom, 2022: Sea ice-free corridors for large swell to reach Antarctic ice shelves. *Environ. Res. Lett.*, **17**, 045026, https://doi.org/10.1088/1748-9326/ac5edd.

Thomas, E. R., and Coauthors, 2017: Regional Antarctic snow accumulation over the past 1000 years. *Climate Past*, **13**, 1491–1513, https://doi.org/10.5194/cp-13-1491-2017.

Thompson-Munson, M., N. Wever, C. M. Stevens, J. T. M. Lenaerts, and B. Medley, 2023: An evaluation of a physics-based firn model and a semi-empirical firn model across the Greenland Ice Sheet (1980–2020). *Cryosphere*, **17**, 2185–2209, https://doi.org/10.5194/tc-17-2185-2023.

Torinesi, O., M. Fily, and C. Genthon, 2003: Variability and trends of the summer melt period of Antarctic ice margins since 1980 from microwave sensors. *J. Climate*, **16**, 1047–1060, https://doi.org/10.1175/1520-0442(2003)016<1047:VATOTS>2.0.CO;2.

Turner, J., and Coauthors, 2019: The dominant role of extreme precipitation events in Antarctic snowfall variability. *Geophys. Res. Lett.*, **46**, 3502–3511, https://doi.org/10.1029/2018GL081517.

——, and Coauthors, 2022a: Record low Antarctic sea ice cover in February 2022. *Geophys. Res. Lett.*, **49**, e2022GL098904, https://doi.org/10.1029/2022GL098904.

——, H. Lu, J. C. King, S. Carpentier, M. Lazzara, T. Phillips, and J. Wille, 2022b: An extreme high temperature event in coastal East Antarctica associated with an atmospheric river and record summer downslope winds. *Geophys. Res. Lett.*, **49**, e2021GL097108, https://doi.org/10.1029/2021GL097108.

Udy, D. G., T. R. Vance, A. S. Kiem, and N. J. Holbrook, 2022: A synoptic bridge linking sea salt aerosol concentrations in East Antarctic snowfall to Australian rainfall. *Commun. Earth Environ.*, **3**, 175, https://doi.org/10.1038/s43247-022-00502-w.

Vance, T. R., and Coauthors, 2016: Optimal site selection for a high-resolution ice core record in East Antarctica. *Climate Past*, **12**, 595–610, https://doi.org/10.5194/cp-12-595-2016.

——, A. S. Kiem, L. M. Jong, J. L. Roberts, C. T. Plummer, A. D. Moy, M. A. J. Curran, and T. D. van Ommen, 2022: Pacific decadal variability over the last 2000 years and implications for climatic risk. *Comm. Earth Environ.*, **3**, 33, https://doi.org/10.1038/s43247-022-00359-z.

Vignon, É., O. Traullé, and A. Berne, 2019: On the fine vertical structure of the low troposphere over the coastal margins of East Antarctica. *Atmos. Chem. Phys.*, **19**, 4659–4683, https://doi.org/10.5194/acp-19-4659-2019.

——, M.-L. Roussel, I. V. Gorodetskaya, C. Genthon, and A. Berne, 2021: Present and future of rainfall in Antarctica. *Geophys. Res. Lett.*, **48**, e2020GL092281, https://doi.org/10.1029/2020GL092281.

Wang, Y., Q. Wu, X. Zhang, and Z. Zhai, 2023: Record-breaking Antarctic snowfall in 2022 delays global sea level rise. *Sci. Bull.*, https://doi.org/10.1016/j.scib.2023.08.055, in press.

Wever, N., E. Keenan, C. Amory, M. Lehning, A. Sigmund, H. Huwald, and J. T. M. Lenaerts, 2022: Observations and simulations of new snow density in the drifting snow-dominated environment of Antarctica. *J. Glaciol.*, **69**, 823–840, https://doi.org/10.1017/jog.2022.102.

Wille, J. D., V. Favier, A. Dufour, I. V. Gorodetskaya, J. Turner, C. Agosta, and F. Codron, 2019: West Antarctic surface melt triggered by atmospheric rivers. *Nat. Geosci.*, **12**, 911–916, https://doi.org/10.1038/s41561-019-0460-1.

——, and Coauthors, 2021: Antarctic atmospheric river climatology and precipitation impacts. *J. Geophys. Res. Atmos.*, **126**, e2020JD033788, https://doi.org/10.1029/2020JD033788.

——, and Coauthors, 2022: Intense atmospheric rivers can weaken ice shelf stability at the Antarctic Peninsula. *Commun. Earth Environ.*, **3**, 90, https://doi.org/10.1038/s43247-022-00422-9.

——, and Coauthors, 2024: The extraordinary March 2022 East Antarctica "heat" wave. Part I: Observations and meteorological drivers. *J. Climate*, **37**, 757–778.